2019-08-19

Wave diffraction from multiple truncated cylinders of arbitrary cross sections

Zheng, S

10.1016/j.apm.2019.08.006
Applied Mathematical Modelling
Elsevier BV

Title:
Wave diffraction from multiple truncated cylinders of arbitrary cross sections

Author names and affiliations:
Siming Zheng[a,b], Yongliang Zhang[b], Jiabin Liu[c], Gregorio Iglesias[d,a]

a *School of Engineering, University of Plymouth, Drake Circus, Plymouth PL4 8AA, UK*
b *State Key Laboratory of Hydroscience and Engineering, Tsinghua University, Beijing 100084, China*
c *Key Lab of Structures Dynamic Behavior and Control of the Ministry of Education, Harbin Institute of Technology, Harbin, 150090, China*
d *MaREI, Environmental Research Institute & School of Engineering, University College Cork, Ireland*

E-mail address:
Siming Zheng[a,b] siming.zheng@plymouth.ac.uk/zhengsm@tsinghua.edu.cn
Yongliang Zhang[b] yongliangzhang@tsinghua.edu.cn
Jiabin Liu[c] jliu448@aucklanduni.ac.nz
Gregorio Iglesias[d,a] gregorio.iglesias@ucc.ie

Corresponding author: Gregorio Iglesias
E-mail address: gregorio.iglesias@ucc.ie

Received 28 January 2019, Revised 30 July 2019, Accepted 12 August 2019, Available online 19 August 2019.

DOI: 10.1016/j.apm.2019.08.006

Wave diffraction from multiple truncated cylinders of arbitrary cross sections

Abstract: Many marine structures are supported by piles or caissons which, from a mathematical point of view, can be assimilated to an array of truncated cylinders of arbitrary cross sections. The focus of this paper is such an array subjected to harmonic waves of small steepness. We develop an analytic method based on linear potential flow theory to solve the diffraction problem and evaluate the excitation forces and moments acting on each cylinder. The water domain is divided into the interior regions below each cylinder and an exterior region extending to infinity in the horizontal plane. A series of eigen-functions are applied to express the velocity potential in each region. The Fourier series method combined with the eigen-function expansion matching method is used to satisfy the wetted surface body conditions and continuity conditions between adjacent regions. The analytic model is validated by comparing its results with numerical modelling results and published data. It is then applied to two truncated cylinders with caisson cross sections, and results are given for the excitation forces and moments on each cylinder for different values of incident wave direction and spacing between the cylinders, and for different configurations.

Keywords: Wave diffraction; Wave excitation force; Wave-structure interaction; Truncated cylinders; Potential flow; Analytical model

1. Introduction

There are many offshore structures that are composed of an array of cylinders, e.g., marine drilling platforms, floating airports, bridge pylons, offshore wind farms and wave farms [1]. For this reason the study of wave diffraction by multiple cylinders has sparked tremendous interest from engineers and researchers. When the cylinders in the array are far away from one another, the hydrodynamic interaction between them may be expected to be negligible; in such circumstances, the wave forces acting on each cylinder in the array are similar to those acting on an isolated cylinder.

Wave diffraction by a single cylinder with circular cross section has been widely investigated. As early as 1971, Garrett [2] expanded an incident plane wave using Bessel functions and conducted an analytic study on the scattering of waves by a circular dock, in which a series of eigen-functions were applied to express the velocity potential and calculate wave forces. Black, Mei and Bray [3] applied Haskind's theorem to evaluate the wave forces acting on a fixed vertical truncated circular cylinder, which can be either partially immersed in the free surface or resting on the seabed with its height completely submerged, with only far-field properties. The vertical wave force acting on the floating truncated cylinder was seen to approach the additional hydrostatic force when the wave number tended to zero due to the free surface elevation, whereas the vertical force acting on the bottom-mounted cylinder became negligible as the wave number tended to zero, for the cylinder had a vanishing water plane area. Wave diffraction from a circular cylinder in other situations, e.g., located over a cylindrical barrier, floating in water of infinite depth, located in front of a vertical wall, horizontal and submerged, were extensively investigated [4-15] and brief reviews of the diffraction problems can also be found in our previous work [11, 12, 16].

In addition to the case of a cylinder of circular cross section, wave diffraction from a cylinder of elliptic cross section has also attracted some attention. The exact analytic solution of wave diffraction by a bottom-mounted, surface-piercing elliptic cylinder was first presented by Chen

and Mei [17]. In their study, the governing Laplace equation was expressed in elliptic cylindrical coordinates; therefore, the fluid velocity potential was written in terms of infinite series of Mathieu functions. This complete solution was considered too complex and costly for engineering applications[18]. To reduce the time required by the complete solution, Williams [18] presented two approximate solutions for the diffraction problem and the calculation of the wave excitation forces and moments on the surface-piercing elliptic cylinder. For a stationary cylinder of elliptic shape, partially immersed, the hydrodynamic loading was analytically investigated by Chen and Mei [19] based on linearized shallow water wave theory and adopting a depth-averaged velocity potential, i.e., the velocity potentials in each region of the fluid domain were bidimensional, without consideration of the vertical coordinate in the matching procedure (2DH). The shallow-water theory was also employed by Williams [20] to study diffraction from a stationary elliptic breakwater either partially immersed or totally submerged and resting on the sea-bed. Later, these problems were re-investigated without the shallow-water restriction [21]; therefore, in addition to the angular coordinates, the vertical coordinate was retained in the analysis. The theoretical solution of the interaction of linearized waves with a submerged horizontal disk of elliptic cross section can be found in Zhang and Williams [22].

As regards cylinders with other cross-sections, a cosine-type cross-section was investigated by Mansour, Williams and Wang [23], who presented a leading order analytic solution for a uniform, bottom-mounted, surface-piercing cylinder based on a perturbation theory, in terms of the amplitude of the perturbation from a circular cross-section. Their analytic results were found to be in good agreement with numerical results only for small values of the perturbation amplitude. More recently, the linear wave diffraction by a vertical, uniform, surface piercing cylinder with an arbitrary smooth cross-section was analytically solved by Liu, Guo and Li [24], Liu, Guo, Fang, Li, Hu and Liu [25]. The Fourier series method combined with the Galerkin method were used to satisfy the wetted surface body conditions and continuity conditions between adjacent subdomains. Alternatively, Dişibűyűk, Korobkin and Yilmaz [26] solved wave diffraction from a uniform vertical cylinder of arbitrary cross section by using an asymptotic approach, in which a fifth-order asymptotic expansion of the velocity potential was substituted in the boundary condition. The agreement between their theoretical predictions of the hydrodynamic forces and wave run-up and those from Liu, Guo and Li [24] was shown to be fairly good.

For the majority of offshore structures that can be assimilated to an array of cylinders of arbitrary cross-sections, in practice, the spacing between the cylinders is typically not large enough for hydrodynamic interactions to be ignored; it follows that the wave excitation forces and moments acting on each cylinder are strongly affected by the waves diffracted from the others [27].

To analyse the hydrodynamic interaction occurring between multiple circular cylinders, Kagemoto and Yue [28], Alliney [29] developed an interaction theory, which can be used to predict wave exciting forces given only the diffraction characteristics of individual members. This theory was also extended by Yilmaz and Incecik [30], Yilmaz [31] and Siddorn and Eatock Taylor [32] to solve the problems of wave diffraction and radiation from an array of truncated vertical circular cylinders. Linton and Evans [33] applied a direct method to wave diffraction problem of multiple circular uniform cylinders and obtained new formulae for the wave excitation forces and free-surface elevation close to a particular cylinder. Recently, Zheng and Zhang [34] presented a theoretical study on a hybrid wave energy converter, in which an analytic model was proposed to

solve the problems of wave diffraction and radiation from a hollow cylinder and a surrounding array of solid cylinders. Analytic solutions of the hydrodynamic problems from a hybrid wave farm consisting of an array of truncated cylinders with and without moonpools were derived as well [35]. Other studies regarding wave diffraction of circular cylinders can be found in the review presented by Eatock Taylor [36].

With regard to an array of elliptic uniform cylinders, Chatjigeorgiou and Mavrakos [37] presented a semi-analytic model for the hydrodynamic diffraction. In their model, the Mathieu function addition theorem was adopted and properly extended so that it can be expressed in terms of the even and odd periodic and radial Mathieu functions. Later, Chatjigeorgiou [38] provided an analytic solution of hydrodynamic interactions between elliptic and circular uniform cylinders, in which the circular cylinders were considered as different geometries rather than special cases of elliptic cylinders with zero elliptic eccentricity. The theoretical model is more comprehensive, requiring the implementation of both Mathieu and Bessel functions; in exchange, this approach allows for efficient and accurate computations. Chatjigeorgiou [39] extended the research work by Chatjigeorgiou and Mavrakos [37] to multiple elliptic truncated cylinders. Chen and Lee [40] solved wave scattering from an array of four identical elliptical cylinders in a semi-analytical manner. Both physical (near-trapped mode) and mathematical (fictitious frequency) resonances were observed in their study. More recently, Zheng, Zhang, Liu and Iglesias [41] presented a semi-analytic model to solve the problem of wave radiation from cylinders with arbitrary cross sections oscillating independently in the absence of an incident wave.

To the authors' best knowledge, there has been no analytic research work reported on wave scattering from an array of cylinders with arbitrary cross sections – a relevant problem in Ocean Engineering, and the subject of this paper. More specifically, we focus on wave diffraction from multiple stationary truncated cylinders partially immersed in the free surface, and propose an analytic model based on linear potential flow theory to solve the diffraction problem and evaluate the excitation forces and moments acting on each cylinder.

2. Mathematical model

The problem geometry is illustrated in Fig. 1. An array of N ($N\geq 2$) vertical cylinders with arbitrary cross sections are partially immersed in water of finite depth h. The draft of cylinder n (n=1,2,…, N) is denoted as d_n. To describe the problem clearly, as shown in Fig. 1a, a Cartesian coordinate system $Oxyz$ is defined with the plane of Oxy coinciding with the still water level (SWL) and the Oz pointing upwards. The multiple cylinders are subjected to a train of regular gravity waves of amplitude A and angular frequency ω incoming at angle β to the positive x-direction. The amplitude A is assumed to be small compared to the wavelength; in other words, wave steepness is assumed to be small. Apart from the $Oxyz$ system, N cylindrical coordinates are employed with the origins set inside the cross section of each cylinder at SWL. The cylindrical coordinate corresponding to cylinder n is denoted as $O_nr_n\theta_nz$ with the origin O_n, located at $(x_n,y_n,0)$ in the $Oxyz$ system. A point (x_n,y_n,z_n) in the $Oxyz$ system is used as the reference point to calculate the wave excitation moments acting on cylinder n. The fluid is divided into N+1 regions (Fig. 1b): the first N regions are the interior regions below each cylinder; Region N+1 denotes the exterior region, extending to infinity in the horizontal plane.

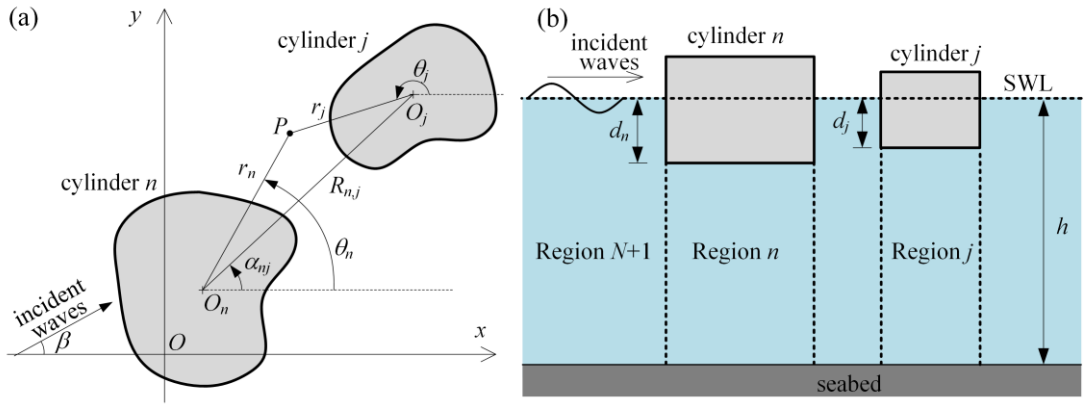

Fig. 1. Definition sketch: (a) plan view; (b) side view

The shape of the cross section of cylinder *n* can be described in its own cylindrical coordinate system $O_n r_n \theta_n z$ as $r_n=R_n(\theta_n)$, which represents the radius of any point at the edge of cross section at θ_n. In order to describe the unit normal vector at the side surface of cylinder *n*, S_n function is introduced as:

$$S_n\left(r_n,\theta_n\right)=r_n-R_n\left(\theta_n\right), \tag{1}$$

in which $S_n=0$ represents the cross section of cylinder *n* as well, and the unit normal vector pointing into the water at the side surface in the $O_n r_n \theta_n z$ system and the *Oxyz* system can be written as Eqs. (2a) and (2b), respectively[16, 24, 41]:

$$\vec{n}=\frac{1}{\sqrt{1+\left(\frac{1}{r_n}\frac{\partial S_n}{\partial\theta_n}\right)^2}}\left(\vec{e}_{r,n}+\frac{1}{r_n}\frac{\partial S_n}{\partial\theta_n}\vec{e}_{\theta,n}+0\vec{e}_z\right), \tag{2a}$$

$$\vec{n}=\frac{1}{\sqrt{1+\left(\frac{1}{r_n}\frac{\partial S_n}{\partial\theta_n}\right)^2}}\left(\left(\cos\theta_n-\frac{1}{r_n}\frac{\partial S_n}{\partial\theta_n}\sin\theta_n\right)\vec{i}+\left(\sin\theta_n+\frac{1}{r_n}\frac{\partial S_n}{\partial\theta_n}\cos\theta_n\right)\vec{j}+0\vec{k}\right), \tag{2b}$$

where ($\vec{e}_{r,n}$, $\vec{e}_{\theta,n}$, $\vec{e}_z$) are the unit basis vectors in the $O_n r_n \theta_n z$ system, and ($\vec{i}$, $\vec{j}$, $\vec{k}$) are the unit basis vectors in the *Oxyz* system.

Assuming the fluid to be incompressible and inviscid, the irrotational fluid motion excited by regular waves with small amplitude might be described by using linear flow potential theory and the velocity potential can be written as $\varphi(x,y,z,t)=\mathrm{Re}[\Phi(x,y,z)e^{-i\omega t}]$, where *t* is the time, i is the imaginary unit, Φ is a complex spatial velocity potential. It follows that both φ and Φ satisfy the Laplace equation everywhere in the fluid domain.

In the frame of the linear flow theory, the spatial velocity potential Φ can be separated into contributions from the incident wave field and the diffracted field as:

$$\Phi=\Phi_{\mathrm{I}}+\Phi_{\mathrm{D}}, \tag{3}$$

where Φ_{I} and Φ_{D} represent the incident wave spatial potential and the diffracted one, respectively. Both of them satisfy the Laplace equation.

Generally, the velocity spatial potential for the undisturbed incident waves is well known and

Φ_{I} in the $O_n r_n \theta_n z$ system can be written as [34, 35]:

$$\Phi_{\mathrm{I}} = -\frac{\mathrm{i}gA}{\omega}\frac{\cosh\left[k_0\left(z+h\right)\right]}{\cosh\left(k_0 h\right)}\mathrm{e}^{\mathrm{i}k_0\left(x_n\cos\beta+y_n\sin\beta\right)}\sum_{m=-\infty}^{\infty}\mathrm{i}^m\mathrm{e}^{-\mathrm{i}m\beta}J_m\left(k_0 r_n\right)\mathrm{e}^{\mathrm{i}m\theta_n}, \tag{4}$$

where k_0 is the wave number satisfying the dispersion relation $\omega^2=gk_0\tanh(k_0h)$, in which g is the gravity acceleration; J_m is the Bessel function of order m.

The boundary conditions for Φ_{D} can be written as follows:

1) The linear free surface condition:

$$\frac{\partial\Phi_{\mathrm{D}}}{\partial z}-\frac{\omega^2}{g}\Phi_{\mathrm{D}}=0, \qquad z=0 \ \text{ and } \ r_n\geq R_n \tag{5}$$

2) The non-penetrating condition on the seabed:

$$\frac{\partial\Phi_{\mathrm{D}}}{\partial z}=0, \qquad z=-h \tag{6}$$

3) The surface condition at the wetted surface of each cylinder:

$$\frac{\partial\Phi_{\mathrm{D}}}{\partial z}=-\frac{\partial\Phi_{\mathrm{I}}}{\partial z}, \qquad z=-d_n \ \text{ and } \ 0\leq r_n\leq R_n \tag{7}$$

$$\frac{\partial\Phi_{\mathrm{D}}}{\partial n}=-\frac{\partial\Phi_{\mathrm{I}}}{\partial n}, \qquad -d_n\leq z\leq 0 \ \text{ and } \ r_n=R_n \tag{8}$$

4) The radiation condition at infinity:

$$\sqrt{k_0 r_n}\left(\frac{\partial\Phi_{\mathrm{D}}}{\partial r_n}-\mathrm{i}k_0\Phi_{\mathrm{D}}\right)=0, \qquad r_n\to\infty \tag{9}$$

3 Solution to diffracted potentials

The diffracted spatial potential in Region n is denoted as $\Phi_{\mathrm{D},n}$. The method of separation of variables is applied in each region in order to obtain expressions for the unknown diffracted potentials.

3.1 Diffracted spatial potentials in different regions

1) Region n (n=1,2, …, N)

The diffracted spatial potential in Region n can be written in the $O_n r_n \theta_n z$ system as

$$\Phi_{\mathrm{D},n}\left(r_n,\theta_n,z\right)=\Phi_{\mathrm{D},n,\mathrm{p}}+\sum_{m=-\infty}^{\infty}\left[A_{m,0}^{\mathrm{D},n}\left(r_n\right)^{|m|}+\sum_{l=1}^{\infty}A_{m,l}^{\mathrm{D},n}I_m\left(\beta_{n,l}r_n\right)\cos\left[\beta_{n,l}\left(z+h\right)\right]\right]\mathrm{e}^{\mathrm{i}m\theta_n}, \tag{10}$$

where $A_{m,l}^{\mathrm{D},n}$ are unknown coefficients to be solved in Section 3.2; I_m is the modified Bessel function of first kind and order m; $\beta_{n,l}$ is the eigenvalue which is given by

$$\beta_{n,l}=\frac{l\pi}{h-d_n}, \quad l=0, 1, 2, 3,\ldots, \tag{11}$$

$\Phi_{\mathrm{D},n,\mathrm{p}}$ is a particular solution, $\Phi_{\mathrm{D},n,\mathrm{p}}=-\Phi_{\mathrm{I}}$.

2) Region N+1

In Region N+1, i.e., the exterior domain, the diffracted spatial potential can be decomposed into the contributions from the waves diffracted from the N cylinders:

$$\Phi_{\mathrm{D},N+1}=\sum_{n=1}^{N}\Phi_{n}^{\mathrm{D,e}}, \tag{12}$$

in which $\Phi_{n}^{\mathrm{D,e}}$ represents the diffracted potential corresponding to the waves travelling outwards from cylinder n and can be written in terms of eigen-function expansion in the $O_nr_n\theta_nz$ system as:

$$\Phi_{n}^{\mathrm{D,e}}\left(r_n,\theta_n,z\right)=\sum_{m=-\infty}^{\infty}\left[B_{m,0}^{\mathrm{D},n}H_m\left(k_0r_n\right)\frac{Z_0\left(z\right)}{Z_0\left(0\right)}+\sum_{l=1}^{\infty}B_{m,l}^{\mathrm{D},n}K_m\left(k_lr_n\right)\frac{Z_l\left(z\right)}{Z_l\left(0\right)}\right]\mathrm{e}^{\mathrm{i}m\theta_n} \tag{13}$$

where

$$Z_0\left(z\right)=N_0^{-1/2}\cosh\left[k_0\left(z+h\right)\right];\quad Z_l\left(z\right)=N_l^{-1/2}\cos\left[k_l\left(z+h\right)\right]; \tag{14}$$

$$N_0=\frac{1}{2}\left[1+\frac{\sinh\left(2k_0h\right)}{2k_0h}\right];\quad N_l=\frac{1}{2}\left[1+\frac{\sin\left(2k_lh\right)}{2k_lh}\right]; \tag{15}$$

$B_{m,l}^{\mathrm{D},n}$ are the unknown coefficients to be solved in Section 3.2; H_m is the Hankel function of first kind of order m; K_m is the modified Bessel function of second kind of order m; k_l is the eigenvalue which is given by

$$\omega^2=-k_lg\tan\left(k_lh\right),\qquad l=1,2,3,\ldots \tag{16}$$

With the employment of Graf's addition theorem for Bessel functions [11, 12, 28, 32, 34, 42], $\Phi_{j}^{\mathrm{D,e}}$ can be expressed in different cylindrical coordinate systems, and when $r_n\le R_{jn}$, Eq. (12) can be rewritten in the $O_nr_n\theta_nz$ system as:

$$\begin{aligned}\Phi_{\mathrm{D},N+1}\left(r_n,\theta_n,z\right)=&\sum_{m=-\infty}^{\infty}\left[B_{m,0}^{\mathrm{D},n}H_m\left(k_0r_n\right)\frac{Z_0\left(z\right)}{Z_0\left(0\right)}+\sum_{l=1}^{\infty}B_{m,l}^{\mathrm{D},n}K_m\left(k_lr_n\right)\frac{Z_l\left(z\right)}{Z_l\left(0\right)}\right]\mathrm{e}^{\mathrm{i}m\theta_n}\\&+\sum_{\substack{j=1\\j\neq n}}^{N}\sum_{m=-\infty}^{\infty}\left\{B_{m,0}^{\mathrm{D},j}\frac{Z_0\left(z\right)}{Z_0\left(0\right)}\sum_{m'=-\infty}^{\infty}\left(-1\right)^{m'}H_{m-m'}\left(k_0R_{jn}\right)J_{m'}\left(k_0r_n\right)\mathrm{e}^{\mathrm{i}\left(m\alpha_{jn}-m'\alpha_{nj}\right)}\mathrm{e}^{\mathrm{i}m'\theta_n}\right.\\&\left.+\sum_{l=1}^{\infty}B_{m,l}^{\mathrm{D},j}\frac{Z_l\left(z\right)}{Z_l\left(0\right)}\sum_{m'=-\infty}^{\infty}K_{m-m'}\left(k_lR_{jn}\right)I_{m'}\left(k_lr_n\right)\mathrm{e}^{\mathrm{i}\left(m\alpha_{jn}-m'\alpha_{nj}\right)}\mathrm{e}^{\mathrm{i}m'\theta_n}\right\}\end{aligned} \tag{17}$$

3.2 Method of computation for unknown coefficients

The unknown coefficients in Eqs. (10), (13) and (17) can be determined by using the conditions of continuity of pressure and mass flux at $r_n=R_n$ (n=1,2,…, N):

1) Continuity of pressure at the boundary S_n=0:

$$\Phi_{\mathrm{D},N+1}\big|_{S_n=0}=\Phi_{\mathrm{D},n}\big|_{S_n=0},\qquad -h<z<-d_n. \tag{18}$$

2) Continuity of mass flux at the boundary S_n=0:

$$\left.\frac{\partial \Phi_{\mathrm{D},N+1}\left(r_n,\theta_n,z\right)}{\partial n}\right|_{S_n=0}=\begin{cases}\left.-\dfrac{\partial \Phi_{\mathrm{I}}\left(r_n,\theta_n,z\right)}{\partial n}\right|_{S_n=0}, & -d_n<z<0\\ \left.\dfrac{\partial \Phi_{\mathrm{D},n}\left(r_n,\theta_n,z\right)}{\partial n}\right|_{S_n=0}, & -h<z<-d_n\end{cases}, \tag{19a}$$

which, with the employment of Eq. (2a), can be further expressed in the frame of the local cylindrical coordinate system $O_n r_n \theta_n z$ as

$$\left.\left(r_n^2\frac{\partial \Phi_{\mathrm{D},N+1}}{\partial r_n}+\frac{\partial S_n}{\partial \theta_n}\frac{\partial \Phi_{\mathrm{D},N+1}}{\partial \theta_n}\right)\right|_{S_n=0}=\begin{cases}\left.-\left(r_n^2\dfrac{\partial \Phi_{\mathrm{I}}}{\partial r_n}+\dfrac{\partial S_n}{\partial \theta_n}\dfrac{\partial \Phi_{\mathrm{I}}}{\partial \theta_n}\right)\right|_{S_n=0}, & -d_n<\mathrm{z}<0\\ \left.\left(r_n^2\dfrac{\partial \Phi_{\mathrm{D},n}}{\partial r_n}+\dfrac{\partial S_n}{\partial \theta_n}\dfrac{\partial \Phi_{\mathrm{D},n}}{\partial \theta_n}\right)\right|_{S_n=0}, & -h<\mathrm{z}<-d_n\end{cases}. \tag{19b}$$

After inserting the expressions of the wave diffracted spatial potential as given in Eqs. (10) and (17) into Eqs. (18) and (19b), the terms with r_n and $\partial S_n/\partial\theta_n$ at S_n=0 are both found to be dependent on θ_n, and can be expanded into a Fourier series as follows [41]:

$$J_m\left(k_0 r_n\right)\big|_{S_n=0}=\sum_{q=-\infty}^{\infty} f_{m,0,q}^{J,n}\mathrm{e}^{\mathrm{i}q\theta_n};\ \left.\left(r_n^2 k_0 J_m'\left(k_0 r_n\right)+\mathrm{i}mJ_m\left(k_0 r_n\right)\frac{\partial S_n}{\partial\theta_n}\right)\right|_{S_n=0}=\sum_{q=-\infty}^{\infty} f_{m,0,q}^{J',n}\mathrm{e}^{\mathrm{i}q\theta_n} \tag{20a}$$

$$H_m\left(k_0 r_n\right)\big|_{S_n=0}=\sum_{q=-\infty}^{\infty} f_{m,0,q}^{H,n}\mathrm{e}^{\mathrm{i}q\theta_n};\ \left.\left(r_n^2 k_0 H_m'\left(k_0 r_n\right)+\mathrm{i}mH_m\left(k_0 r_n\right)\frac{\partial S_n}{\partial\theta_n}\right)\right|_{S_n=0}=\sum_{q=-\infty}^{\infty} f_{m,0,q}^{H',n}\mathrm{e}^{\mathrm{i}q\theta_n} \tag{20b}$$

$$K_m\left(k_l r_n\right)\big|_{S_n=0}=\sum_{q=-\infty}^{\infty} f_{m,l,q}^{K,n}\mathrm{e}^{\mathrm{i}q\theta_n};\ \left.\left(r_n^2 k_l K_m'\left(k_l r_n\right)+\mathrm{i}mK_m\left(k_l r_n\right)\frac{\partial S_n}{\partial\theta_n}\right)\right|_{S_n=0}=\sum_{q=-\infty}^{\infty} f_{m,l,q}^{K',n}\mathrm{e}^{\mathrm{i}q\theta_n} \tag{20c}$$

$$I_m\left(k_l r_n\right)\big|_{S_n=0}=\sum_{q=-\infty}^{\infty} f_{m,l,q}^{I,n}\mathrm{e}^{\mathrm{i}q\theta_n};\ \left.\left(r_n^2 k_l I_m'\left(k_l r_n\right)+\mathrm{i}mI_m\left(k_l r_n\right)\frac{\partial S_n}{\partial\theta_n}\right)\right|_{S_n=0}=\sum_{q=-\infty}^{\infty} f_{m,l,q}^{I',n}\mathrm{e}^{\mathrm{i}q\theta_n} \tag{20d}$$

$$I_m\left(\beta_{n,l} r_n\right)\big|_{S_n=0}=\sum_{q=-\infty}^{\infty} \tilde{f}_{m,l,q}^{I,n}\mathrm{e}^{\mathrm{i}q\theta_n};\left.\left(r_n^2\beta_{n,l} I_m'\left(\beta_{n,l} r_n\right)+\mathrm{i}mI_m\left(\beta_{n,l} r_n\right)\frac{\partial S_n}{\partial\theta_n}\right)\right|_{S_n=0}=\sum_{q=-\infty}^{\infty} \tilde{f}_{m,l,q}^{I',n}\mathrm{e}^{\mathrm{i}q\theta_n} \tag{20e}$$

$$\left(r_n\right)^{|m|}\big|_{S_n=0}=\sum_{q=-\infty}^{\infty} f_{m,0,q}^{R,n}\mathrm{e}^{\mathrm{i}q\theta_n};\ \left.\left(|m|\left(r_n\right)^{|m|+1}+\mathrm{i}m\left(r_n\right)^{|m|}\frac{\partial S_n}{\partial\theta_n}\right)\right|_{S_n=0}=\sum_{q=-\infty}^{\infty} \tilde{f}_{m,0,q}^{R,n}\mathrm{e}^{\mathrm{i}q\theta_n} \tag{20f}$$

for n=1…N, where the Fourier coefficients on the right-hand side of Eqs. (20a)~(20f), represented by $\Re_{n,q}$ for convenience, can be obtained from

$$\Re_{n,q}=\frac{1}{2\pi}\int_{-\pi}^{\pi}\Psi_{n,q}\left(\theta_n\right)\mathrm{e}^{-\mathrm{i}q\theta_n}\mathrm{d}\theta_n, \tag{21}$$

in which $\Psi_{n,q}$ denotes the θ_n dependent items as given at the left side of Eqs. (20a)~(20f).

The orthogonal properties of the functions cos$n\theta$, sin$n\theta$, and $Z_l(z)$ can also be used by multiplying Eqs. (18) and (19) with $\mathrm{e}^{-\mathrm{i}\tau\theta_n}\cos\left[\beta_{n,\varsigma}\left(z+h\right)\right]/\left(h-d_n\right)$ and $\mathrm{e}^{-\mathrm{i}\tau\theta_n}Z_\varsigma/h$,

respectively, on both sides and integrating with respect to θ and z, as follows:

$$\begin{aligned}&\int_{-\pi}^{\pi}\left[\int_{-h}^{-d_n}\Phi_{\mathrm{D},N+1}\left(r_n,\theta_n,z\right)\Big|_{S_n=0}\frac{\cos\left[\beta_{n,\varsigma}\left(z+h\right)\right]}{h-d_n}\mathrm{d}z\right]\mathrm{e}^{-\mathrm{i}\tau\theta_n}\mathrm{d}\theta_n\\&=\int_{-\pi}^{\pi}\left[\int_{-h}^{-d_n}\Phi_{\mathrm{D},n}\left(r_n,\theta_n,z\right)\Big|_{S_n=0}\frac{\cos\left[\beta_{n,\varsigma}\left(z+h\right)\right]}{h-d_n}\mathrm{d}z\right]\mathrm{e}^{-\mathrm{i}\tau\theta_n}\mathrm{d}\theta_n\end{aligned},\tag{22}$$

$$\begin{aligned}&\int_{-\pi}^{\pi}\left[\int_{-h}^{0}\frac{\partial\Phi_{\mathrm{D},N+1}\left(r_n,\theta_n,z\right)}{\partial n}\Big|_{S_n=0}\frac{Z_\varsigma\left(z\right)}{h}\mathrm{d}z\right]\mathrm{e}^{-\mathrm{i}\tau\theta_n}\mathrm{d}\theta_n\\&=\int_{-\pi}^{\pi}\left[\int_{-h}^{-d_n}\frac{\partial\Phi_{\mathrm{D},n}\left(r_n,\theta_n,z\right)}{\partial n}\Big|_{S_n=0}\frac{Z_\varsigma\left(z\right)}{h}\mathrm{d}z-\int_{-d_n}^{0}\frac{\partial\Phi_{\mathrm{I}}\left(r_n,\theta_n,z\right)}{\partial n}\Big|_{S_n=0}\frac{Z_\varsigma\left(z\right)}{h}\mathrm{d}z\right]\mathrm{e}^{-\mathrm{i}\tau\theta_n}\mathrm{d}\theta_n\end{aligned},\tag{23}$$

in which τ is an integer which varies from minus infinity to plus infinity, and ζ is an integer varying from zero to plus infinity.

Substituting the expressions for the wave diffracted spatial potential in Eqs. (10) and (17), inserting the Fourier coefficients in Eqs. (20a)~(20f) into Eqs. (22) and (23), and making some rearrangements, we have

$$\begin{aligned}&-\sum_{m=-\infty}^{\infty}\Lambda_{m,\tau,\varsigma}^{1,n}A_{m,\varsigma}^{\mathrm{D},n}+\sum_{m=-\infty}^{\infty}\sum_{l=0}^{\infty}B_{m,l}^{\mathrm{D},n}L_{l,\varsigma}^{(n)}\Lambda_{m,\tau,l}^{2,n}+\sum_{\substack{j=1\\j\neq n}}^{N}\sum_{m=-\infty}^{\infty}\sum_{l=0}^{\infty}B_{m,l}^{\mathrm{D},j}L_{l,\varsigma}^{(n)}T_{m,\tau,l}^{n,j}\\&=\frac{\mathrm{i}gA}{\omega}L_{0,\varsigma}^{(n)}\mathrm{e}^{\mathrm{i}k_0\left(x_n\cos\beta+y_n\sin\beta\right)}\sum_{m=-\infty}^{\infty}\mathrm{i}^m\mathrm{e}^{-\mathrm{i}m\beta}f_{m,0,\tau-m}^{J,n}\end{aligned},\tag{24}$$

$$\begin{aligned}&-\frac{h-d_n}{h}Z_\varsigma\left(0\right)\sum_{m=-\infty}^{\infty}\sum_{l=0}^{\infty}A_{m,l}^{\mathrm{D},n}L_{\varsigma,l}^{(n)}\Lambda_{m,\tau,l}^{3,n}+\sum_{m=-\infty}^{\infty}B_{m,\varsigma}^{\mathrm{D},n}\Lambda_{m,\tau,\varsigma}^{4,n}+\sum_{\substack{j=1\\j\neq n}}^{N}\sum_{m=-\infty}^{\infty}B_{m,\varsigma}^{\mathrm{D},j}T\prime_{m,\tau,\varsigma}^{n,j}\\&=\frac{\mathrm{i}gA}{\omega}\frac{\delta_{0,\varsigma}}{Z_0\left(0\right)}\mathrm{e}^{\mathrm{i}k_0\left(x_n\cos\beta+y_n\sin\beta\right)}\sum_{m=-\infty}^{\infty}\mathrm{i}^m\mathrm{e}^{-\mathrm{i}m\beta}f_{m,0,\tau-m}^{J',n}\end{aligned},\tag{25}$$

where

$$\Lambda_{m,\tau,\varsigma}^{1,n}=\begin{cases}f_{m,\varsigma,\tau-m}^{R,n}, & \varsigma=0\\\dfrac{1}{2}\tilde{f}_{m,\varsigma,\tau-m}^{I,n}, & \varsigma=1,2,3,\ldots\end{cases}\quad\Lambda_{m,\tau,l}^{2,n}=\begin{cases}f_{m,0,\tau-m}^{H,n}, & l=0\\f_{m,l,\tau-m}^{K,n}, & l=1,2,3,\ldots\end{cases},\tag{26}$$

$$\begin{aligned}L_{l,\varsigma}^{(n)}&=\frac{1}{h-d_n}\int_{-h}^{-d_n}\frac{Z_l\left(z\right)\cos\left[\beta_{n,\varsigma}\left(z+h\right)\right]}{Z_l\left(0\right)}\mathrm{d}z\\&=\begin{cases}\dfrac{\left(-1\right)^\varsigma\left(h-d_n\right)k_0\sinh\left[k_0\left(h-d_n\right)\right]}{\left[\left(h-d_n\right)^2k_0^2+\varsigma^2\pi^2\right]\cosh\left(k_0h\right)} & l=0;\varsigma=0,1,2\cdots\\\dfrac{\left(-1\right)^\varsigma\left(h-d_n\right)k_l\sin\left[k_l\left(h-d_n\right)\right]}{\left[\left(h-d_n\right)^2k_l^2-\varsigma^2\pi^2\right]\cos\left(k_lh\right)} & l=1,2,3\cdots;\varsigma=0,1,2\cdots\end{cases}\end{aligned},\tag{27}$$

$$T_{m,\tau,l}^{n,j}=\begin{cases}\sum_{m'=-\infty}^{\infty}(-1)^{m'}H_{m-m'}\left(k_0R_{jn}\right)f_{m',0,\tau-m'}^{J,n}\mathrm{e}^{\mathrm{i}\left(m\alpha_{jn}-m'\alpha_{nj}\right)}, & l=0\\ \sum_{m'=-\infty}^{\infty}K_{m-m'}\left(k_lR_{jn}\right)f_{m',l,\tau-m'}^{I,n}\mathrm{e}^{\mathrm{i}\left(m\alpha_{jn}-m'\alpha_{nj}\right)}, & l=1,2,3,...\end{cases}, \tag{28}$$

$$\Lambda_{m,\tau,l}^{3,n}=\begin{cases}\tilde{f}_{m,0,\tau-m}^{R,n}, & l=0\\ \tilde{f}_{m,l,\tau-m}^{I',n}, & l=1,2,3,...\end{cases}\quad \Lambda_{m,\tau,\varsigma}^{4,n}=\begin{cases}\dfrac{f_{m,0,\tau-m}^{H',n}}{Z_0\left(0\right)}, & \varsigma=0\\ \dfrac{f_{m,\varsigma,\tau-m}^{K',n}}{Z_\varsigma\left(0\right)}, & \varsigma=1,2,3,...\end{cases}. \tag{29}$$

$$T'^{n,j}_{m,\tau,l}=\begin{cases}\dfrac{1}{Z_0\left(0\right)}\sum_{m'=-\infty}^{\infty}(-1)^{m'}H_{m-m'}\left(k_0R_{jn}\right)f_{m',0,\tau-m'}^{J',n}\mathrm{e}^{\mathrm{i}\left(m\alpha_{jn}-m'\alpha_{nj}\right)}, & l=0\\ \dfrac{1}{Z_l\left(0\right)}\sum_{m'=-\infty}^{\infty}K_{m-m'}\left(k_lR_{jn}\right)f_{m',l,\tau-m'}^{I',n}\mathrm{e}^{\mathrm{i}\left(m\alpha_{jn}-m'\alpha_{nj}\right)}, & l=1,2,3,...\end{cases}, \tag{30}$$

We truncate (2*M*+1) terms (*m*=-*M*,…,0, …, *M*) and (*L*+1) terms (*l*=0,1, …, *L*) in Eqs. (10), (13), (24) and (25) and take (*τ*=-*M*,…,0, …, *M*) and (*ζ*=0,1, …, *L*) in Eqs. (24) and (25) as well, thus a 2*N*(2*M*+1)(*L*+1)-order complex linear equation matrix is obtained, which can be used to calculate the same number of unknown coefficients $A_{m,l}^{\mathrm{D},n}$ and $B_{m,l}^{\mathrm{D},n}$. In the following analytic computations, *M*=15 and *L*=8 are taken so as to obtain accurate results.

4 Wave excitation forces and moments

The hydrodynamic pressure in the flow domain is given by the linearized Bernoulli equation, $p=-\rho\partial\mathrm{Re}[(\Phi_\mathrm{I}+\Phi_\mathrm{D})\mathrm{e}^{-\mathrm{i}\omega t}]/\partial t=\rho\mathrm{Re}[\mathrm{i}\omega(\Phi_\mathrm{I}+\Phi_\mathrm{D})\mathrm{e}^{-\mathrm{i}\omega t}]$, where ρ represents the water density. Therefore, the generalized excitation force on cylinder *n* in Mode *j* (*j*=1~6 represent surge, sway, heave, roll, pitch and yaw, respectively) can be calculated from $\mathrm{Re}\left[F_{\mathrm{e},n}^{(j)}\mathrm{e}^{-\mathrm{i}\omega t}\right]$, where

$$F_{\mathrm{e},n}^{(j)}=-\mathrm{i}\omega\rho\int_{S_n}\left(\Phi_\mathrm{I}+\Phi_\mathrm{D}\right)n_j\mathrm{d}s, \tag{31}$$

in which S_n is the wetted surface of cylinder *n*; $n_1=n_x$, $n_2=n_y$ $n_3=n_z$, $n_4=-(z-z_n)n_y+(y-y_n)n_z$, $n_5=(z-z_n)n_x-(x-x_n)n_z$, $n_6=-(y-y_n)n_x+(x-x_n)n_y$, $\vec{n}=n_x\vec{i}+n_y\vec{j}+n_z\vec{k}$ is the unit normal vector directed into the fluid domain at the cylinder surface, as given in Eq. (2b).

The analytic expressions for the diffracted potentials of the whole computational domain are obtained in Section 3, so the wave excitation forces and moments can be calculated directly from Eq. (31).

5 Model validation

Multiple caissons arise in many offshore projects, such as floating bridges [43] and mobile offshore bases [1]. In this section, the case of two caissons (Fig. 2) is used for validating the analytic model of wave diffraction from multiple truncated cylinders of arbitrary cross sections. Located in water with a depth of *h*=20 m, the two caissons have the same dimensions and a draft d_n=5 m. They are deployed in parallel at a distance from each other *e*=20 m, and are subjected to regular waves propagating at an angle $\beta=\pi/6$.

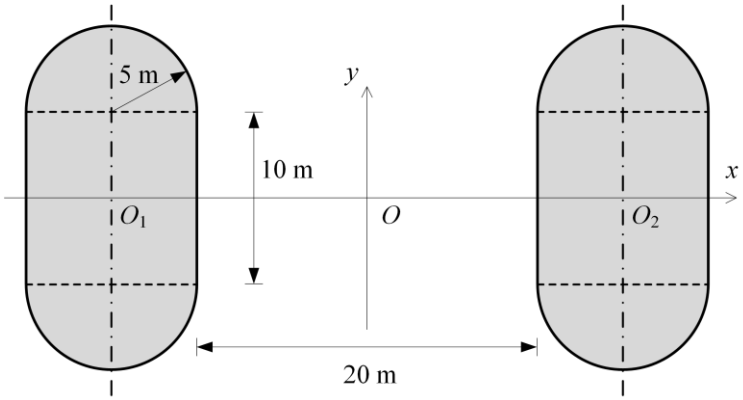

Fig. 2. Top view of the two caissons, case study used for validation.

After solving wave diffraction problem from these caissons, the wave excitation forces and moments obtained are then normalized as follows:

$$\bar{F}_{\mathrm{e},n}^{(j)} = \frac{\left|F_{\mathrm{e},n}^{(j)}\right|}{\rho g A h^{q}}, \qquad q = \begin{cases} 2, & j = 1,2,3 \\ 3, & j = 4,5,6 \end{cases}, \tag{32a}$$

$$\varphi_{\mathrm{e},n}^{(j)} = \arg F_{\mathrm{e},n}^{(j)}. \tag{32b}$$

Hereinafter, k_0 is denoted as k for simplicity, and the nondimensional wave frequency kh is used.

Figures 3 and 4 present a comparison of the present analytic results of wave excitation forces/moments acting on the two caissons (see Fig.2) for different wave frequencies ($0<kh<5.0$) with the numerical results from BEM-based software, ANSYS-AQWA [44]. Figs. 3a and 3b show the wave excitation forces acting on Caisson 1 in terms of dimensionless amplitude and phase angle, respectively. The wave excitation forces acting on Caisson 2 are ploted in Figs. 3c and 3d. Simiarly, the excitation moments loading on Caissons 1 and 2 are illustrated in Figs. 4a~4b and Figs. 4c~4d, respectively.

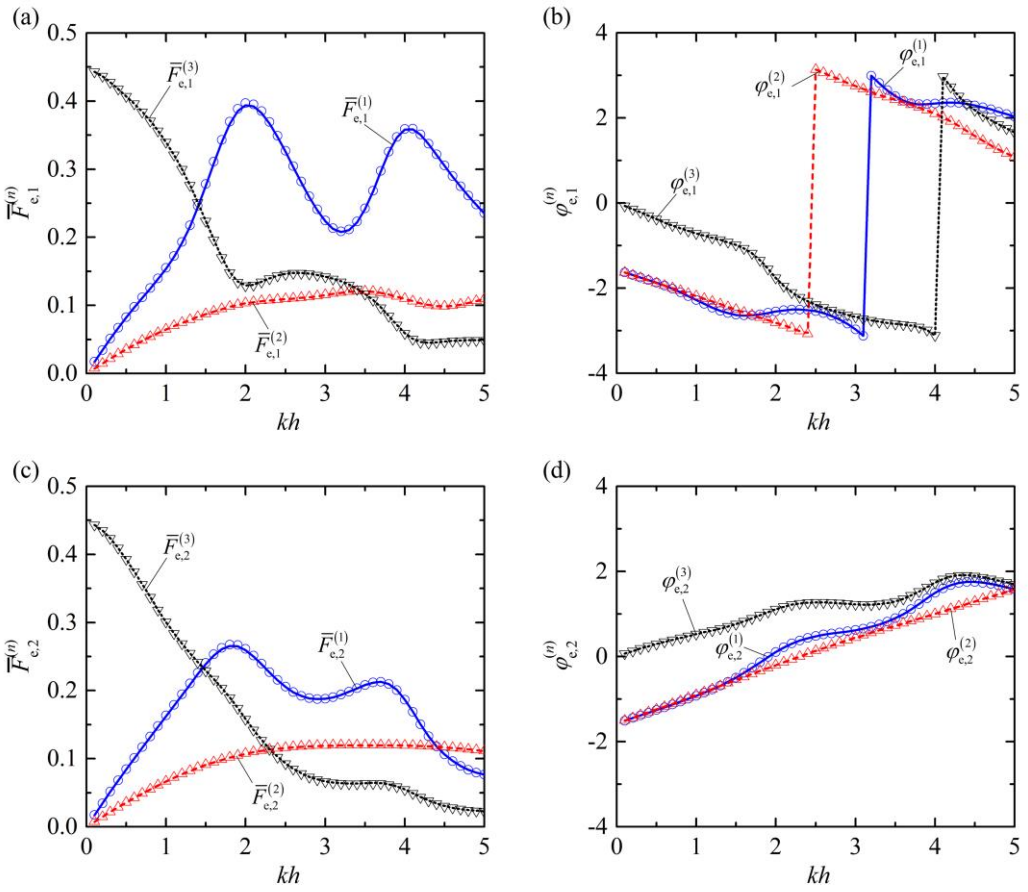

Fig. 3. Comparison of the present analytic results of wave excitation forces acting on the two caissons with the numerical results based on BEM for $\beta=\pi/6$ and $e/h=1.0$: (a) $\overline{F}_{e,1}^{(n)}$, n=1,2,3; (b) $\varphi_{e,1}^{(n)}$, n=1,2,3; (c) $\overline{F}_{e,2}^{(n)}$, n=1,2,3; (d) $\varphi_{e,1}^{(n)}$, n=1,2,3. [Lines: analytic results; symbols: numerical results].

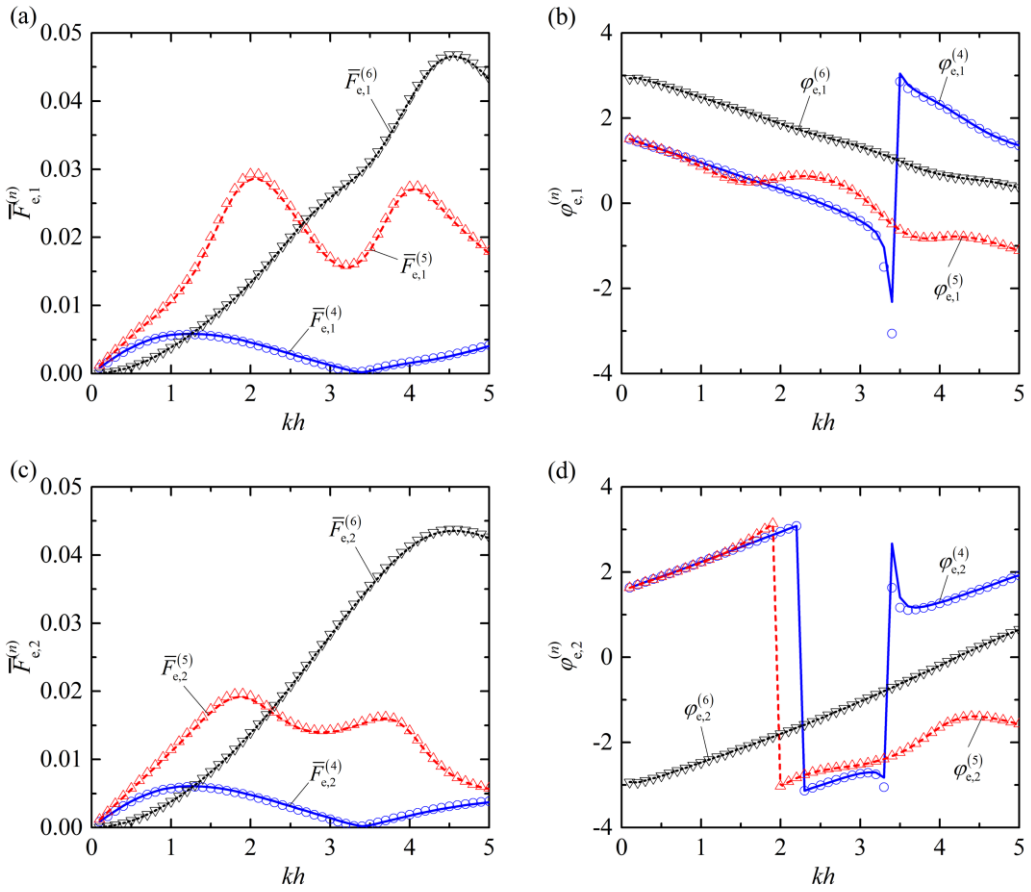

Fig. 4. Comparison of the present analytic results of wave excitation moments acting on the two caissons with the numerical results based on BEM for $\beta=\pi/6$ and $e/h=1.0$: (a) $\bar{F}_{e,1}^{(n)}$, n=4,5,6; (b) $\varphi_{e,1}^{(n)}$, n=4,5,6; (c) $\bar{F}_{e,2}^{(n)}$, n=4,5,6; (d) $\varphi_{e,1}^{(n)}$, n=4,5,6. [Lines: analytic results; symbols: numerical results].

It is shown that the analytic results of the excitation forces and moments acting on each caisson in all modes, i.e., surge, sway, heave, roll, pitch and yaw, fully agree with the numerical results in terms of both dimensionless amplitude and phase angle. This excellent agreement validates the present analytic model.

In addition to the two caissons with a quasi-elliptical cross section, a square array of four identical elliptical cylinders studied analytically by Chen and Lee [40] is selected to validate the present analytic model. All cylinders are fixed on the seabed mounted upward to the free surface. The half lengths of the major and the minor axes of each elliptical cylinder are h and $0.5h$, respectively. The incident wave direction is $\beta=0$. In the present computation, $d_n= 0.98h$ (n=1, 2, 3, 4) was adopted to represent that the cylinders were bottom-mounted. As shown in Fig. 5, the present results of the surge wave excitation forces are in excellent agreement with those in [40].

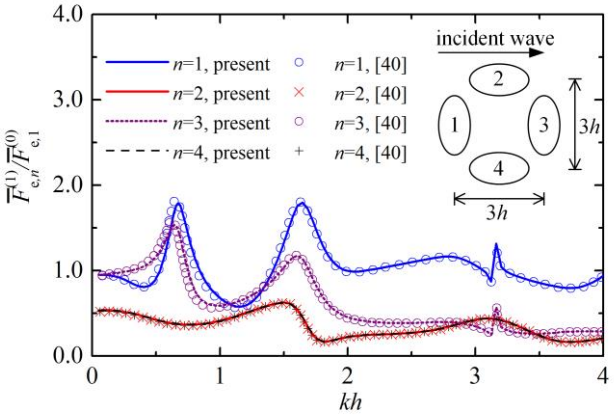

Fig. 5. Comparison of the present analytic results of the surge wave excitation forces acting on each cylinder of an array of four identical elliptical cylinders with the published data [40] for β=0. [$\overline{F}_{e,1}^{(0)}$ denotes the surge wave excitation force acting on the cylinder-1 when it is in isolation]

6 Results and discussion

In this section, the validated analytic model is applied to investigate the role of the incident wave direction, spacing between caissons and configuration angle in the hydrodynamic forces and moments acting on the two caissons depicted in Fig. 2.

6.1 Effect of incident wave angle

The two caissons suffering from incoming regular waves with five different incident wave angles, i.e., β= 0, π/6, π/4, π/3 and π/2, are tested. Figure 6 shows the variations of the excitation forces acting on each caisson in surge, sway and heave modes with kh for different values of β and e/h=1.0. Similarly, the results of the excitation moments in roll, pitch and yaw modes are presented in Fig. 7.

Since both caissons have the same dimensions and are arranged in parallel symmetrically, the results of the excitation forces and moments acting on them in any mode should be the same in terms of amplitude when β = π/2. This is borne out by the results in Figs. 6 and 7.

For β = π/2, the surge excitation force, pitch and yaw excitation moments acting on the isolated induvidual caisson vanish. By contrast, when two caissons are deployed in proximity (Fig. 2), the surge excitation force, and the pitch and yaw excitation moments acting on each caisson may be non-zero due to the hydrodynamic interaction between the caissons. Note that for kh=3.6 and β=π/4, $\overline{F}_{e,1}^{(1)}$ and $\overline{F}_{e,2}^{(1)}$ are 0.056 and 0.282, respectively, implying that, under certain circumstances, the wave excitation forces acting on the leeward caisson can be larger than those acting on the windward caisson.

When incident waves propagate along the x-axis, i.e., β=0, due to the symmetrical property of the two caissons about the plane of y=0, $\overline{F}_{e,n}^{(2)}$, $\overline{F}_{e,n}^{(4)}$ and $\overline{F}_{e,n}^{(6)}$ all vanish (Figs. 6c, 6d, 7a , 7b, 7e and 7f). For kh<3.5, the larger the β, the larger the $\overline{F}_{e,1}^{(2)}$ and $\overline{F}_{e,2}^{(2)}$. This also applies to the effect of β on $\overline{F}_{e,1}^{(4)}$ and $\overline{F}_{e,2}^{(4)}$ for kh<3.5.

β might play opposite roles on $\overline{F}_{e,1}^{(3)}$ for different wave frequencies. For kh<1.0, a larger β results in a smaller $\overline{F}_{e,1}^{(3)}$. Whereas for 1.5<kh<1.8, a larger $\overline{F}_{e,1}^{(3)}$ is obtained for a larger β. For 2.0<kh<5.0, at least one peak of $\overline{F}_{e,1}^{(3)}$-kh occurs for any β studied, except β=π/2. The kh

corresponding to the peaks is rather dependent on β. As a comparison, althouth peaks also appear for $\overline{F}_{e,2}^{(3)}$-kh at 2.0< kh <5.0, the kh values where peaks occur are rather independent of β.

When the caissons are subjected to oblique waves, i.e., β=π/6, π/4 and π/3, $\overline{F}_{e,1}^{(4)}$ and $\overline{F}_{e,2}^{(4)}$ are found to vanish for certain wave conditions (Figs.7a and 7b). Such circumstances are welcome from the standpoint of offshore structures' stability. It may be inferred that the larger the β, the larger the kh where $\overline{F}_{e,1}^{(4)}$ and $\overline{F}_{e,2}^{(4)}$ vanish.

The effect of β on pitch moments is found to be similar to that on surge forces (Figs.7c and 7d). This may be partially due to the position of the rotational reference point, which is located at SWL, implying that the arm of the surge force is generally larger than the arm of the heave force; therefore, the pitch moment is dominated by the part of the surge force acting on the side walls.

Although $\overline{F}_{e,1}^{(6)}$ ($\overline{F}_{e,2}^{(6)}$) is excited for β=π/2 due to hydrodynamic interaction between the caissons, its value is rather small (Figs.7e and 7f). $\overline{F}_{e,1}^{(6)}$ ($\overline{F}_{e,2}^{(6)}$) are mainly excited in oblique incoming waves. For kh <3.8, $\overline{F}_{e,1}^{(6)}$ and $\overline{F}_{e,2}^{(6)}$ for β=π/4 are both larger than the other cases with different value of β.

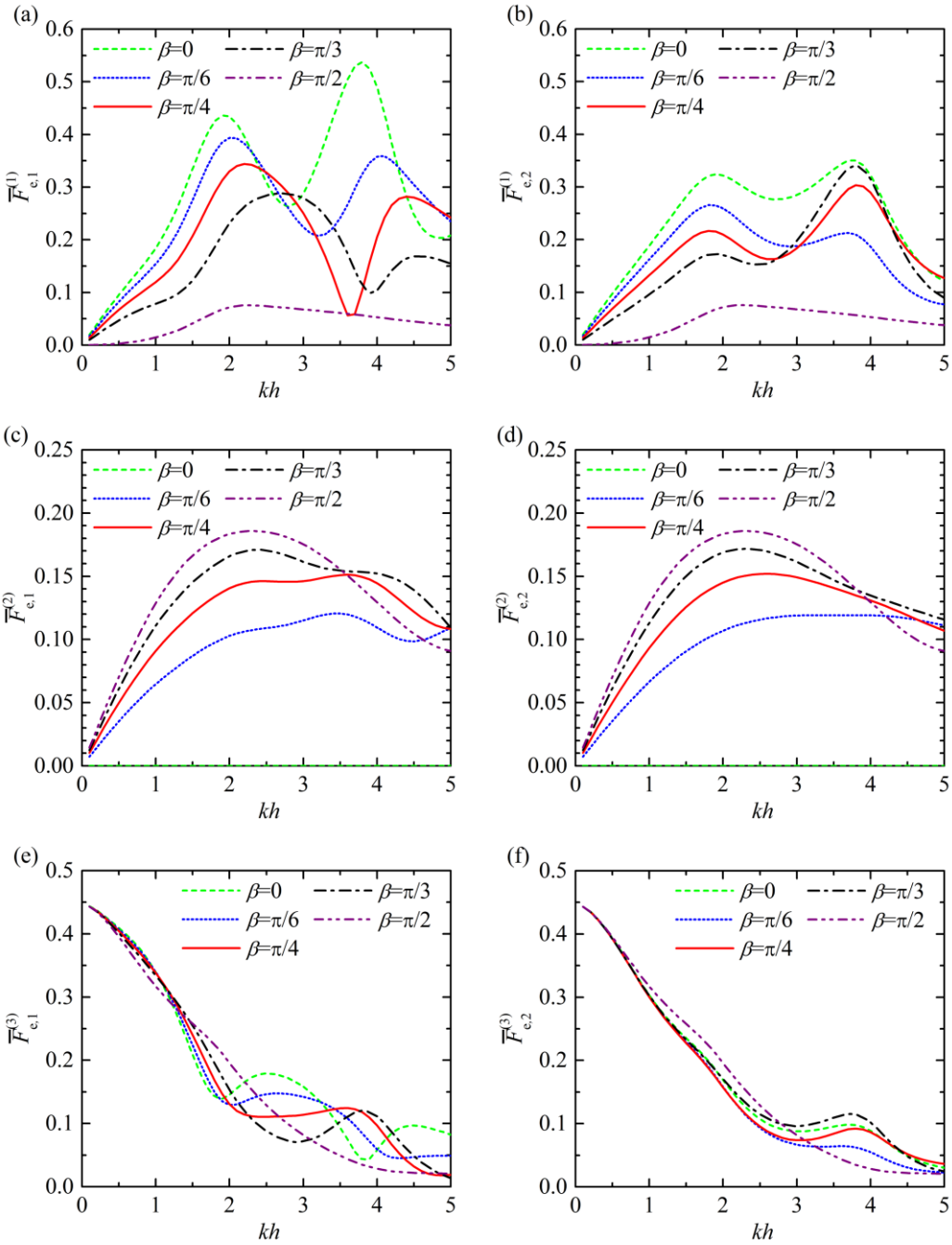

Fig. 6. Normalised wave excitation forces acting on the two caissons vs. *kh* for five incident wave angles: β=0, π/6, π/4, π/3 and π/2 with *e*/*h*=1.0: (a) $\overline{F}_{e,1}^{(1)}$; (b) $\overline{F}_{e,2}^{(1)}$; (c) $\overline{F}_{e,1}^{(2)}$; (d) $\overline{F}_{e,2}^{(2)}$; (e) $\overline{F}_{e,1}^{(3)}$; (f) $\overline{F}_{e,2}^{(3)}$.

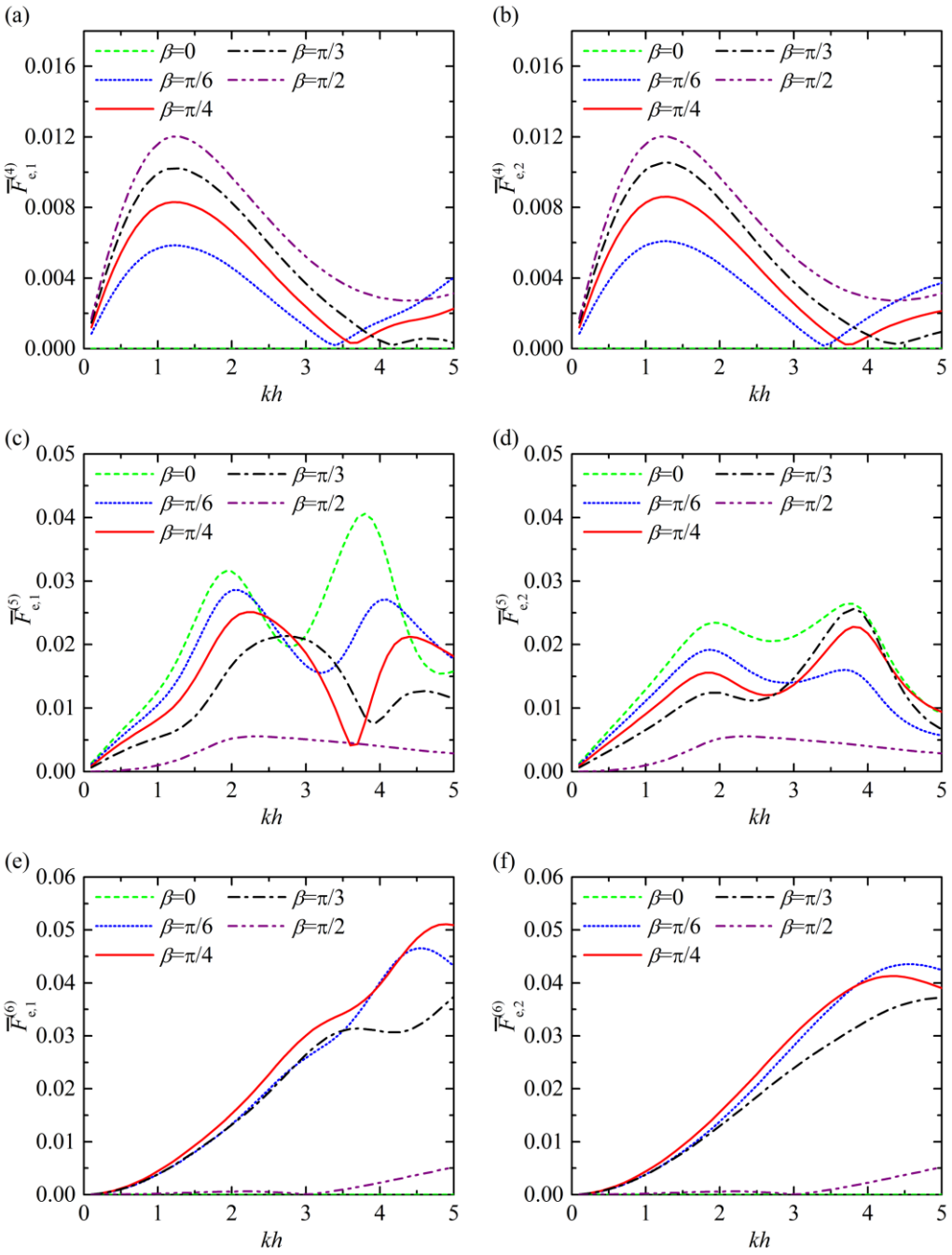

Fig. 7. Normalised wave excitation moments acting on the two caissons vs *kh* for five incident wave angles β=0, π/6, π/4, π/3 and π/2 with *e*/*h*=1.0: (a) $\bar{F}^{(4)}_{e,1}$; (b) $\bar{F}^{(4)}_{e,2}$; (c) $\bar{F}^{(5)}_{e,1}$; (d) $\bar{F}^{(5)}_{e,2}$; (e) $\bar{F}^{(6)}_{e,1}$; (f) $\bar{F}^{(6)}_{e,2}$.

6.2 Effect of spacing between caissons

To study the influence of the spacing between the caissons, *e*, we consider the same two caissons deployed with four different spacings, i.e., *e*/*h*=0.5, 1.0, 1.5 and 2.0, suffering from incoming waves with β=π/6 are studied. In addition, as a comparison, wave diffraction from an individual caisson isolated in open sea is also analytically solved by using the method of [25]. The isolated caisson case is equivalent to the two-caisson case with an extremely large spacing between them, i.e., *e*/*h*=∞, that the hydrodynamic interaction is vanishing. For such case, $\bar{F}^{(i)}_{e,1} = \bar{F}^{(i)}_{e,2}$, *i*=1,2,…,6.

Figures 8 and 9 illustrate the results of excitation forces and moments acting on the caissons, respectively. As shown in Fig. 8a, when the two caissons are placed far away from each other, i.e., the isolated caisson case, the $\bar{F}_{e,1}^{(1)}$ ($\bar{F}_{e,2}^{(1)}$)-*kh* is a one peak curve. While when they are arranged close to each other, e.g., *e*/*h* =0.5~2.0, affected by the reflected waves from Caisson 2, frequency response of the surge excitation force acting on Caisson 1, i.e., $\bar{F}_{e,1}^{(1)}$, is found to oscillate around the $\bar{F}_{e,1}^{(1)}$ -*kh* curve of isolated caisson case. It means that for different wave conditions, $\bar{F}_{e,1}^{(1)}$ can be either strengthened or weakened by the hydrodynamic interaction between the caissons. As *e*/*h* turns larger, strengthening and weakening effects of the hydrodynamic interaction on $\bar{F}_{e,1}^{(1)}$ can switch for a smaller change of *kh*. Different from $\bar{F}_{e,1}^{(1)}$, thanks to the sheltering effect of Caisson 1, $\bar{F}_{e,2}^{(1)}$ is found weakened by hydrodynamic interaction for most wave conditions within *kh* < 5.0 (Fig. 8b). For 3.0 < *kh* < 5.0, $\bar{F}_{e,2}^{(1)}$ with *e*/*h*=0.5 is obviously smaller than the other cases.

As *kh* increases from 0 to 2.5, $\bar{F}_{e,1}^{(2)}$ increases from 0 to 0.11 and there is nearly no influence of *e* on $\bar{F}_{e,1}^{(2)}$ for these wave frequencies (Fig. 8c). As *kh* keeps increasing from 2.5 toward 5.0, $\bar{F}_{e,1}^{(2)}$ for the isolated caisson case stays at a flat level of $\bar{F}_{e,1}^{(2)}$ =1.1. Whereas for the two caissons close to each other, fluctuations of the $\bar{F}_{e,1}^{(2)}$ -*kh* curve around that of the isolated caisson case are observed. The smaller the *e*/*h*, the stronger fluctuations occur. These fluctuations are not found for the sway excitation force acting on Caisson 2 (Fig. 8b). It should be noted that for *kh* <4.0, although Caisson 2 is located at the lee side of Caisson 1, $\bar{F}_{e,2}^{(2)}$ is strengthened by the hydrodynamic interaction. The smaller the *e*/*h*, the larger $\bar{F}_{e,1}^{(2)}$ is obtained.

Similar to the effect of *e* on $\bar{F}_{e,1}^{(1)}$, the $\bar{F}_{e,1}^{(3)}$ -*kh* curves representing two-caisson cases are also observed to oscillate around the curve of isolated caisson case (Fig.8e). As *e*/*h* turns larger, strengthening and weakening effects of the hydrodynamic interaction on $\bar{F}_{e,1}^{(3)}$ switch more frequently for the same range of *kh*. It should be noted that generally the hydrodynamic interaction has opposite effects on $\bar{F}_{e,1}^{(1)}$ and $\bar{F}_{e,1}^{(3)}$, e.g., for the case with *e*/*h* =1.5 at *kh* =3.0, $\bar{F}_{e,1}^{(1)}$ is strengthened whereas $\bar{F}_{e,1}^{(3)}$ is weakened. The heave excitation force acting on Caisson 2, i.e., $\bar{F}_{e,2}^{(3)}$ (Fig. 8f) is affected by *e* in a similar way as $\bar{F}_{e,2}^{(1)}$ is influenced (Fig. 8b).

Both $\bar{F}_{e,1}^{(4)}$ and $\bar{F}_{e,2}^{(4)}$ vanish around *kh* =3.4, regardless of the value of *e*/*h* (Figs.9a and 9b). For *kh* <3.4, $\bar{F}_{e,1}^{(4)}$ is not affected by *e*, neither. Influence of *e* on $\bar{F}_{e,1}^{(4)}$ mainly happens at 4.0< *kh* <5.0, where $\bar{F}_{e,1}^{(4)}$ in the case with *e*/*h* =0.5 is larger than those for the other cases. The results as given in Fig.9b show that $\bar{F}_{e,2}^{(4)}$ is approximately not influenced by *e* unless *e* is rather small, e.g., *e*/*h* =0.5, for which a slightly larger $\bar{F}_{e,2}^{(4)}$ is obtained for *kh* <3.4, whereas an obvious smaller $\bar{F}_{e,2}^{(4)}$ is obtained for *kh* >3.5.

Effect of *e* on $\bar{F}_{e,1}^{(5)}$ and $\bar{F}_{e,2}^{(5)}$ (Figs.9c and 9d) is rather similar to that on $\bar{F}_{e,1}^{(1)}$ and $\bar{F}_{e,2}^{(1)}$ (Figs. 8a and 8b). Hence the description is not repeated here. The yaw moments acting on each caisson, especially those on Caisson 1, are found sensitive to *e* for *kh* >2.5 (Figs.9e and 9f).

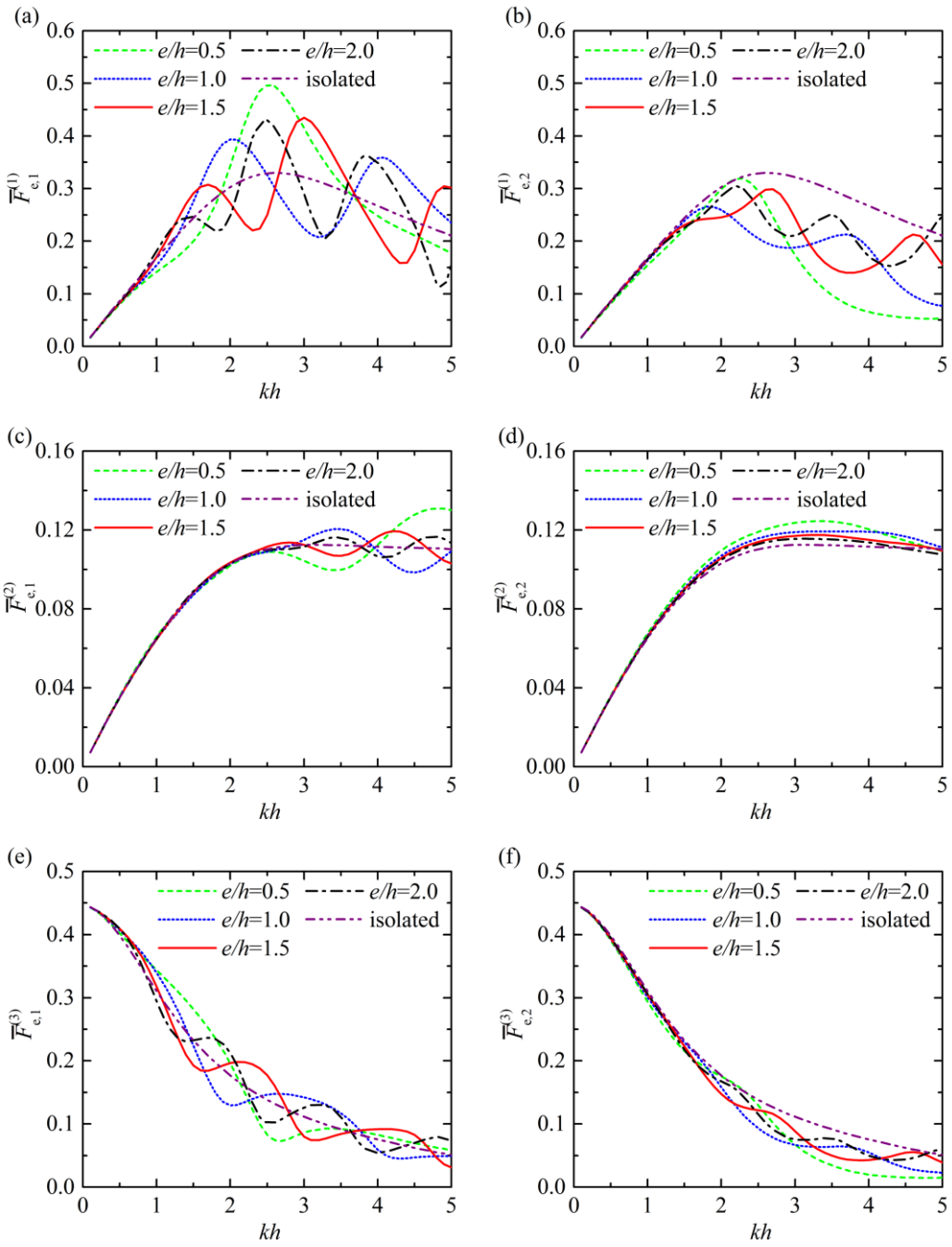

Fig. 8. Normalised wave excitation forces acting on the two caissons vs *kh* for four spacing *e*/*h*=0.5, 1.0, 1.5 and 2.0, together with the isolated case with $\beta=\pi/6$: (a) $\overline{F}^{(1)}_{e,1}$; (b) $\overline{F}^{(1)}_{e,2}$; (c) $\overline{F}^{(2)}_{e,1}$; (d) $\overline{F}^{(2)}_{e,2}$;(e) $\overline{F}^{(3)}_{e,1}$;(f) $\overline{F}^{(3)}_{e,2}$.

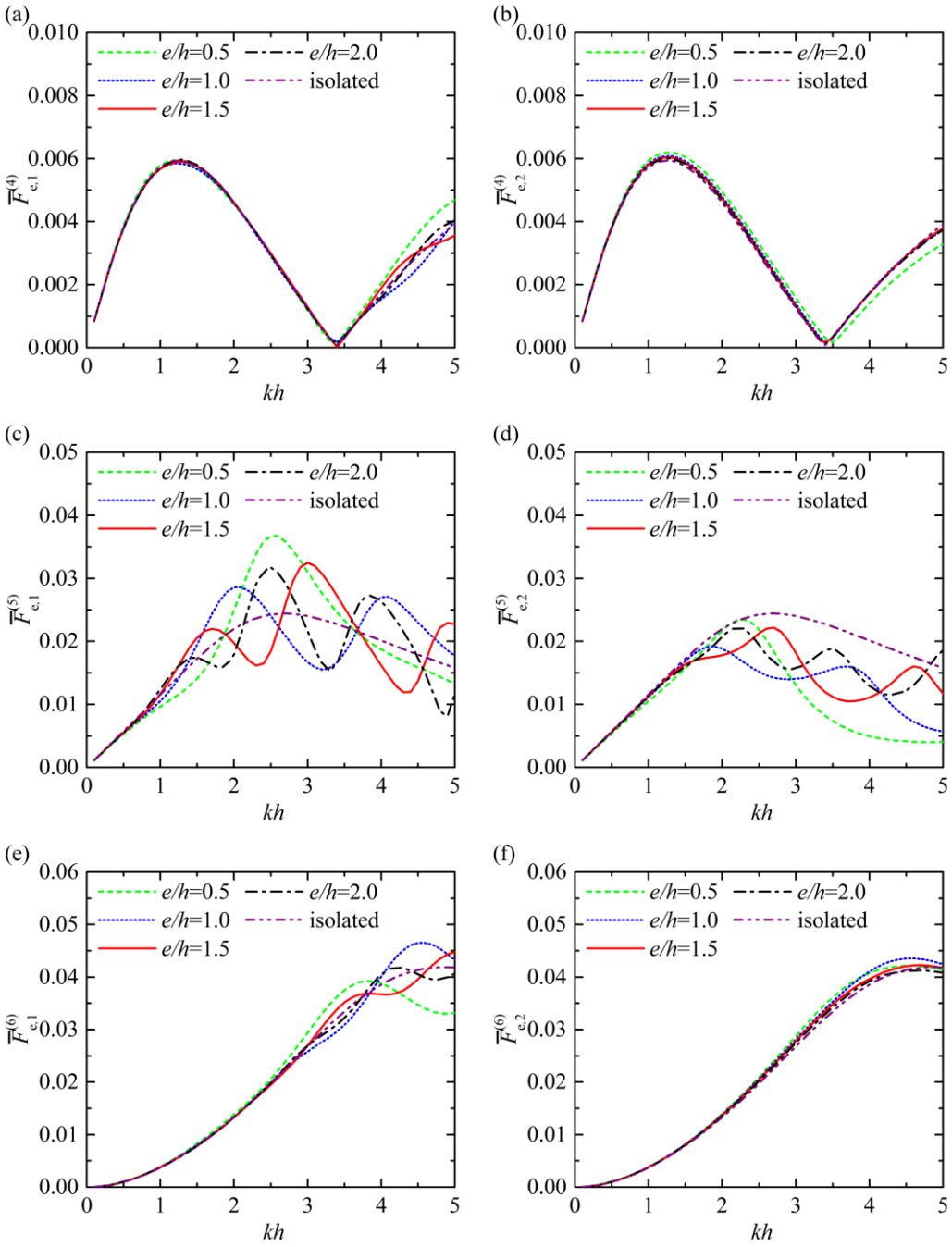

Fig. 9. Normalised wave excitation moments acting on the two caissons vs. kh for four spacings, e/h=0.5, 1.0, 1.5 and 2.0, together with the isolated case with $\beta=\pi/6$: (a) $\overline{F}^{(4)}_{e,1}$; (b) $\overline{F}^{(4)}_{e,2}$; (c) $\overline{F}^{(5)}_{e,1}$; (d) $\overline{F}^{(5)}_{e,2}$; (e) $\overline{F}^{(6)}_{e,1}$; (f) $\overline{F}^{(6)}_{e,2}$.

6.3 Effect of layout

In practice, different configurations of the caissons, e.g., side by side and staggered, will be encountered during the transport and installation process. In this subsection, the layout with the two caissons in parallel at the same distance from their centers is considered. As shown in Fig. 10, the only variable parameter in the different configurations is the angle of the line connecting the caisson centers with the x-axis, which is defined as the configuration angle α.

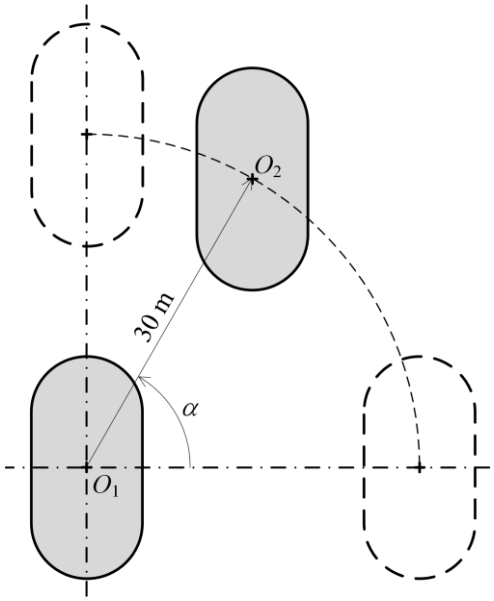

Fig. 10. Definition of the configuration angle α.

The two caissons with α =0, π/6, π/4, π/3 and π/2 subjected to incident waves with β=π/6 are analytically studied. Figures 11 and 12 present the comparison of the results of wave excitation forces and moments, respectively.

As α increases from 0 to π/2, the $\bar{F}_{e,1}^{(1)}$-kh curve changes from double-peaked curve into single-peaked one (Fig.11a). With the increase of α, $\bar{F}_{e,1}^{(1)}$ at kh =2.0 and 4.1 turn smaller and smaller, whereas $\bar{F}_{e,1}^{(1)}$ at kh=3 gets larger and larger, revealing that opposite effects of α on $\bar{F}_{e,1}^{(1)}$ might happen for different wave conditions. While for all the wave conditions examined, except few wave frequencies around kh=4.0, a larger α generally results in a larger $\bar{F}_{e,2}^{(1)}$ (Fig.11b).

In the five cases with α increasing from 0 to π/2, the value of $\bar{F}_{e,1}^{(2)}$ could change a lot for some specified wave conditions (Fig.11c). Take kh=2.6 as an example, $\bar{F}_{e,1}^{(2)}$ for α=π/4 is only 0.082, whereas for α=π/2, $\bar{F}_{e,1}^{(2)}$ reaches 0.154, which is approximately two times as large as that when α=π/4. Similar significant difference of $\bar{F}_{e,2}^{(2)}$ induced by variation of α can be observed for most wave conditions within 2.0<kh<5.0 (Fig.11d). Among the five cases with different values of α, the cases with α=π/2 and π/3 give the maximum and minimum values of $\bar{F}_{e,2}^{(2)}$, respectively, for most wave conditions. For kh ranging from 3.0 to 5.0, the maximum value of $\bar{F}_{e,2}^{(2)}$ is always two times as large as that of the minimum approximately.

For 1.2<kh<2.1, $\bar{F}_{e,1}^{(3)}$ with α=π/2 is the largest among the result in the five cases (Fig.11e). While for 2.4< kh <3.5, on the contrary, $\bar{F}_{e,1}^{(3)}$ with α=π/2 turns to be the smallest one. As a comparison, $\bar{F}_{e,2}^{(3)}$ is maximized and minimized when α=π/2 and α=0, respectively, for any wave conditions at 1.9<kh<5.0 (Fig.11f).

For 1.0<kh<1.7, $\bar{F}_{e,1}^{(4)}$ with α=π/2 is much smaller than any of the other four cases, whereas for kh>2.2, $\bar{F}_{e,1}^{(4)}$ of such case turns to be the largest one (Fig.12a). Whatever the value of α is, a minimum value of $\bar{F}_{e,1}^{(4)}$ occurs around kh=3.3. While the kh corresponding to the minimum value of $\bar{F}_{e,2}^{(4)}$ is a bit more sensitive to the variation of α, e.g., the kh corresponding to the minimum of $\bar{F}_{e,2}^{(4)}$ for α=π/3 and π/2 are 3.0 and 3.6, respectively. For kh ranging from 1.3 to 3.1, $\bar{F}_{e,2}^{(4)}$ for the cases with α=π/3 and π/2 are always the smallest and largest ones, respectively, among the five cases.

The frequency response curves of $\bar{F}_{e,1}^{(5)}$ and $\bar{F}_{e,2}^{(5)}$ for different α (Figs. 12c and 12d) are

found to be similar to those of $\bar{F}_{e,1}^{(1)}$ and $\bar{F}_{e,2}^{(1)}$ in Figs. 11a and 11b. The discussion of the effect of α on $\bar{F}_{e,1}^{(1)}$ and $\bar{F}_{e,2}^{(1)}$ can be applied to $\bar{F}_{e,1}^{(5)}$ and $\bar{F}_{e,2}^{(5)}$ as well.

Figures 12e and 12f illustrate the results of $\bar{F}_{e,1}^{(6)}$ and $\bar{F}_{e,2}^{(6)}$. For kh>2.5, compared with the other four cases, $\bar{F}_{e,2}^{(6)}$ with α=0 is much larger and deserves more attention for stability.

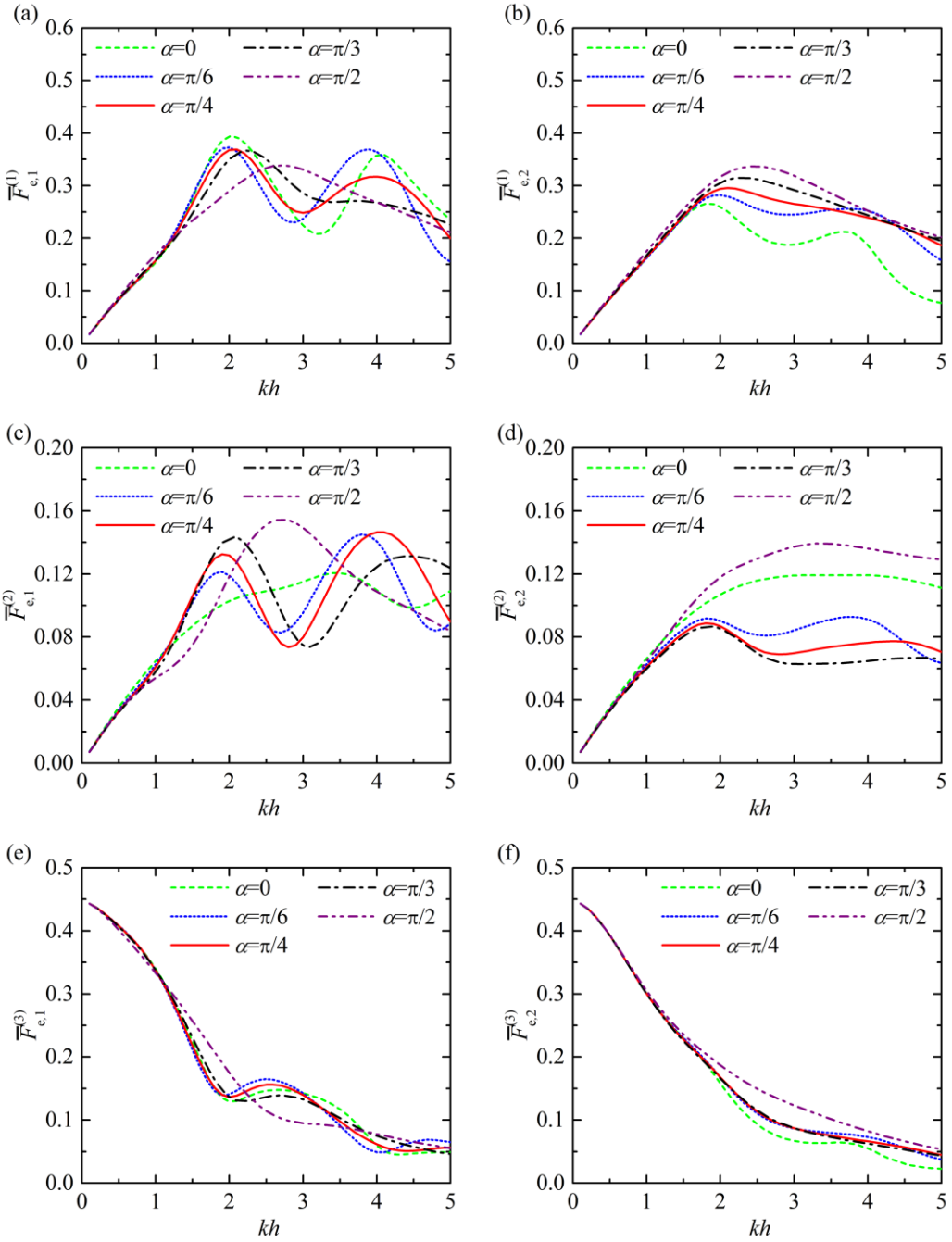

Fig. 11. Normalised wave excitation forces acting on the two caissons vs kh for different configuration angle α =0, π/6, π/4, π/3 and π/2 with β=π/6: (a) $\bar{F}_{e,1}^{(1)}$; (b) $\bar{F}_{e,2}^{(1)}$; (c) $\bar{F}_{e,1}^{(2)}$; (d) $\bar{F}_{e,2}^{(2)}$; (e) $\bar{F}_{e,1}^{(3)}$; (f) $\bar{F}_{e,2}^{(3)}$.

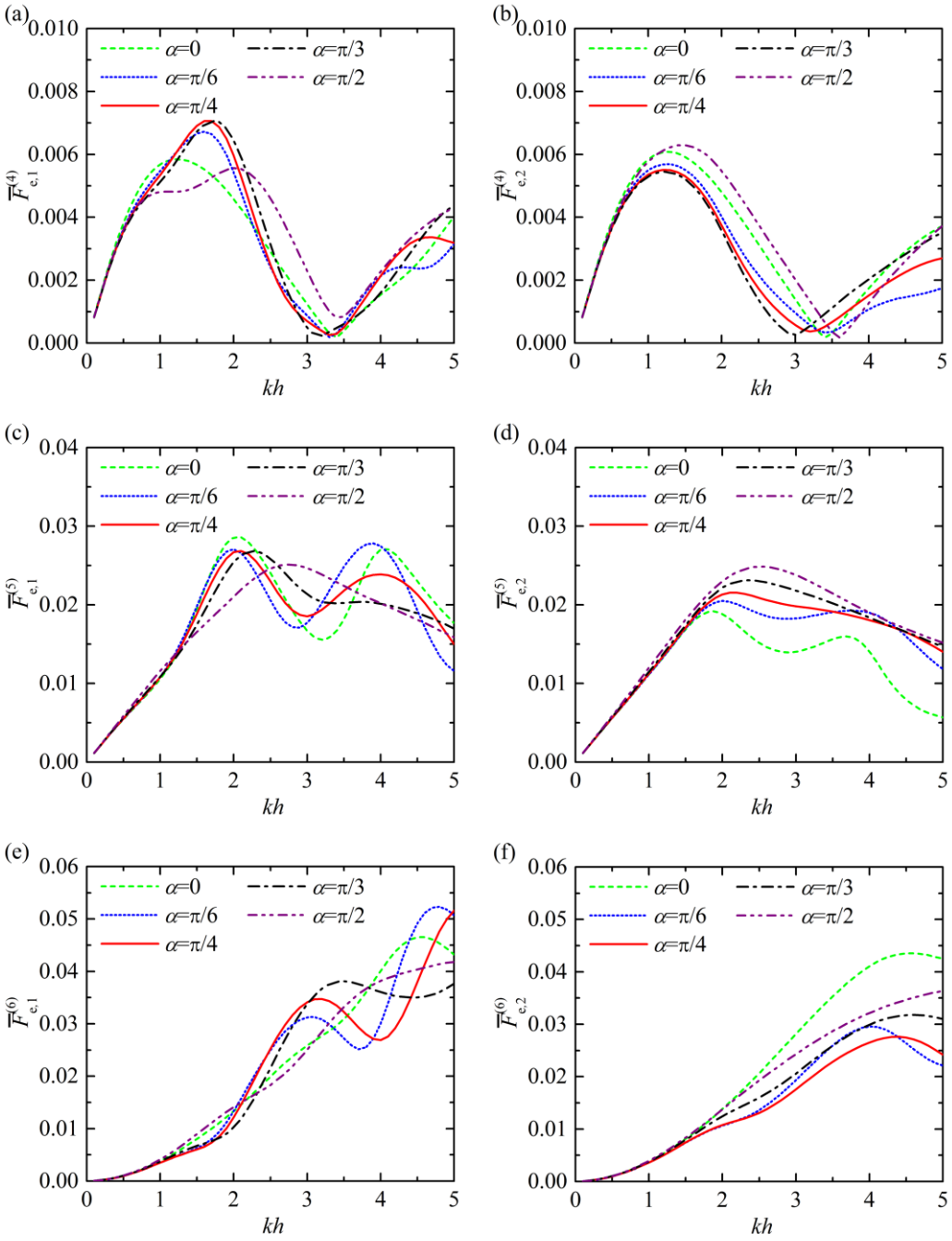

Fig. 12. Normalised wave excitation moments acting on the two caissons vs *kh* for different configuration angle α =0, π/6, π/4, π/3 and π/2 with β=π/6: (a) $\overline{F}^{(4)}_{e,1}$; (b) $\overline{F}^{(4)}_{e,2}$; (c) $\overline{F}^{(5)}_{e,1}$; (d) $\overline{F}^{(5)}_{e,2}$; (e) $\overline{F}^{(6)}_{e,1}$; (f) $\overline{F}^{(6)}_{e,2}$.

6.4 Effect of the shape of cross section

To examine the effect of the shape of the cross section of the cylinders, we consider two identical caissons with a similar deployment to Fig. 2, and with the same horizontal distance between the centroids of 30 m, but with different cross sections. More specifically, four cross sections are examined (Fig. 13a; only one caisson is plotted), in which κ and κ' represent the ratios of the lengths of the two straight edge sections relative to the corner radius, R_0 (Fig. 13b). All these cross sections have the same area. Note κ' is set to zero unless otherwise specified. As κ

increases from 0, the cross section evolves from circular into quasi-elliptical with its major axis in parallel with the y-axis. The larger the κ, the slenderer the shape. The exact size of the cross section for the case κ=2 can be found in Fig. 2. For κ=κ'=2, the cross section turns into a square with circular corners. The caisson draft of all these four cases d_n=5 m, water depth h=20 m, and incident wave direction β =π/6.

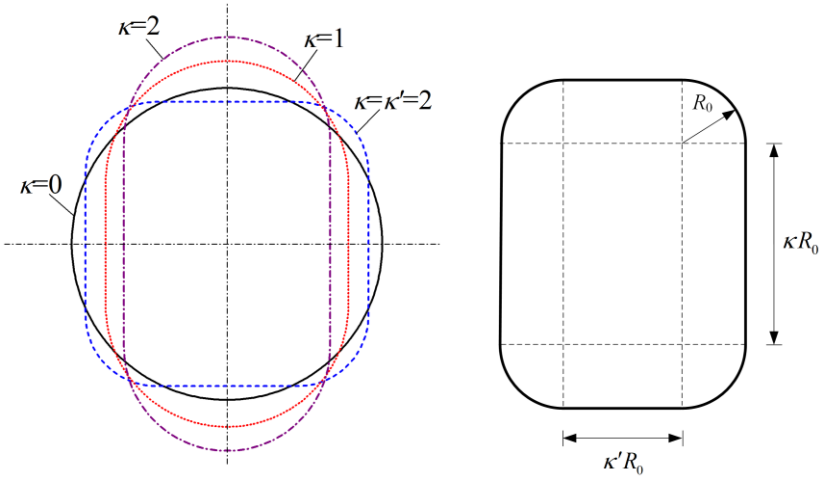

Fig. 13. (left) Schematic of the four shapes of cross section; (right) Definition of κ and κ'.

Figure 14 shows the variation with kh of the excitation forces acting on each caisson in surge, sway and heave modes for different shapes of cross section. Results of the excitation moments acting on each caisson in roll, pitch and yaw modes are given in Fig. 15.

Since the caissons in the case κ=2 are the slenderest among the four cases, the wave excitation forces/moments acting on each caisson in this case in surge, pitch and yaw modes are the largest among the case studies for the majority of the wave frequencies tested, and the wave excitation forces in the sway mode are the smallest. Similar curves representing the surge and heave wave excitation forces, together with the pitch excitation moment acting on each caisson for cases κ=0 and κ=κ'=2 are observed (Figs. 14a, 14b, 14e, 14f, 15c and 15d). Although the length of the caissons in the case κ=κ'=2 along the x-axis is smaller than the case κ=0, $\bar{F}_{e,1}^{(2)}$ and $\bar{F}_{e,2}^{(2)}$ for case κ=κ'=2 are the largest for all the wave frequencies tested (Figs.14 c and 14d). In long waves, e.g., kh<2.0, the wave excitation forces acting on each caisson in heave mode are nearly independent of the shape of the cross sections with the same area (Figs. 14e and 14f). For 2.0<kh<3.8 a larger $\bar{F}_{e,1}^{(3)}$ can be obtained for the case with a larger κ and κ'=0.

As shown in Figs.15a and 15b, $\bar{F}_{e,1}^{(4)}$ and $\bar{F}_{e,2}^{(4)}$ for cases κ=1 and 2 vanish for certain wave conditions. As a comparison, $\bar{F}_{e,1}^{(4)}$ and $\bar{F}_{e,2}^{(4)}$ for cases κ=0 and κ=κ'=2 never vanish for the entire range of wave frequencies tested. Moreover, $\bar{F}_{e,1}^{(4)}$ and $\bar{F}_{e,2}^{(4)}$ for case κ=κ'=2 are larger compared to case κ=0 for the whole range of computed wave conditions. As expected, the yaw excitation moments vanish for circular caissons, i.e., case κ=0 (Fig. 15e and 15f).

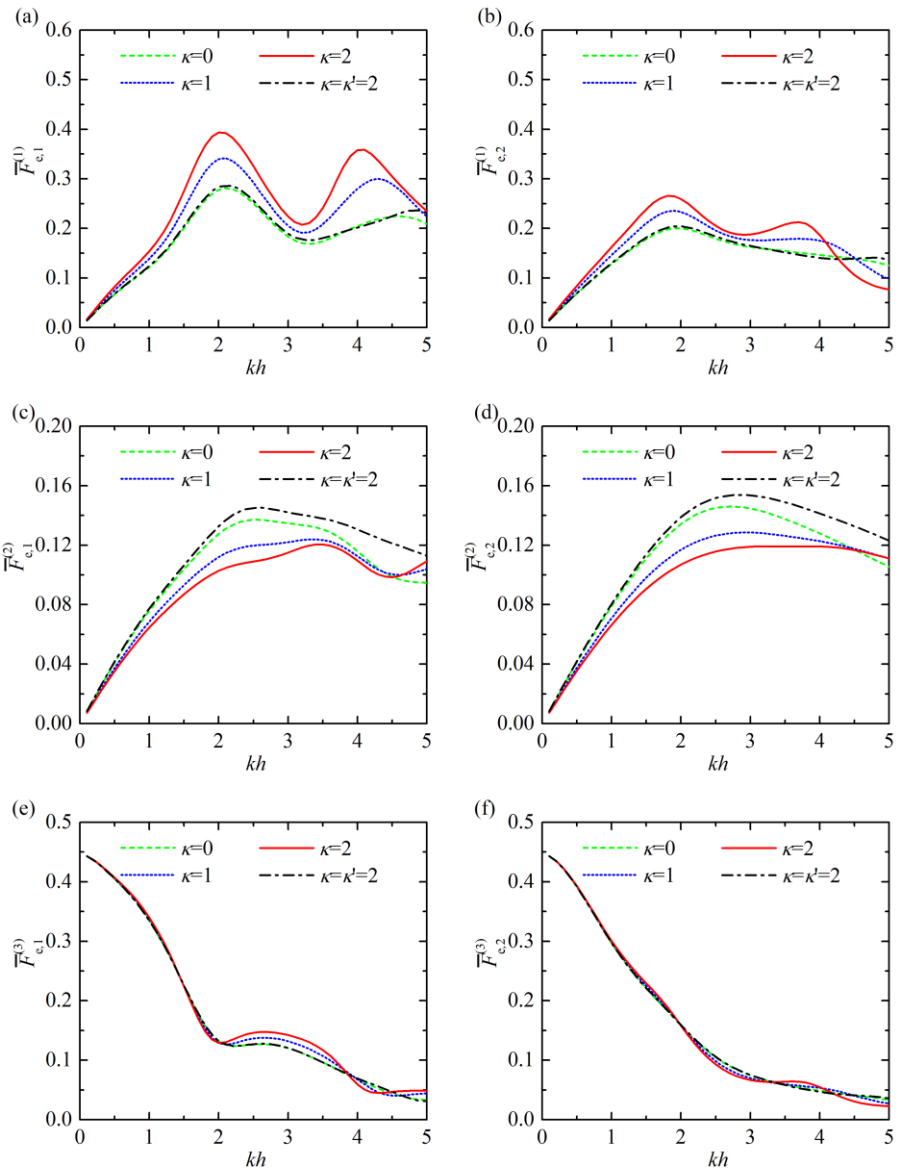

Fig. 14. Normalised wave excitation forces acting on the two caissons vs. *kh* for four shapes of cross section: (a) $\overline{F}^{(1)}_{e,1}$; (b) $\overline{F}^{(1)}_{e,2}$; (c) $\overline{F}^{(2)}_{e,1}$; (d) $\overline{F}^{(2)}_{e,2}$; (e) $\overline{F}^{(3)}_{e,1}$; (f) $\overline{F}^{(3)}_{e,2}$.

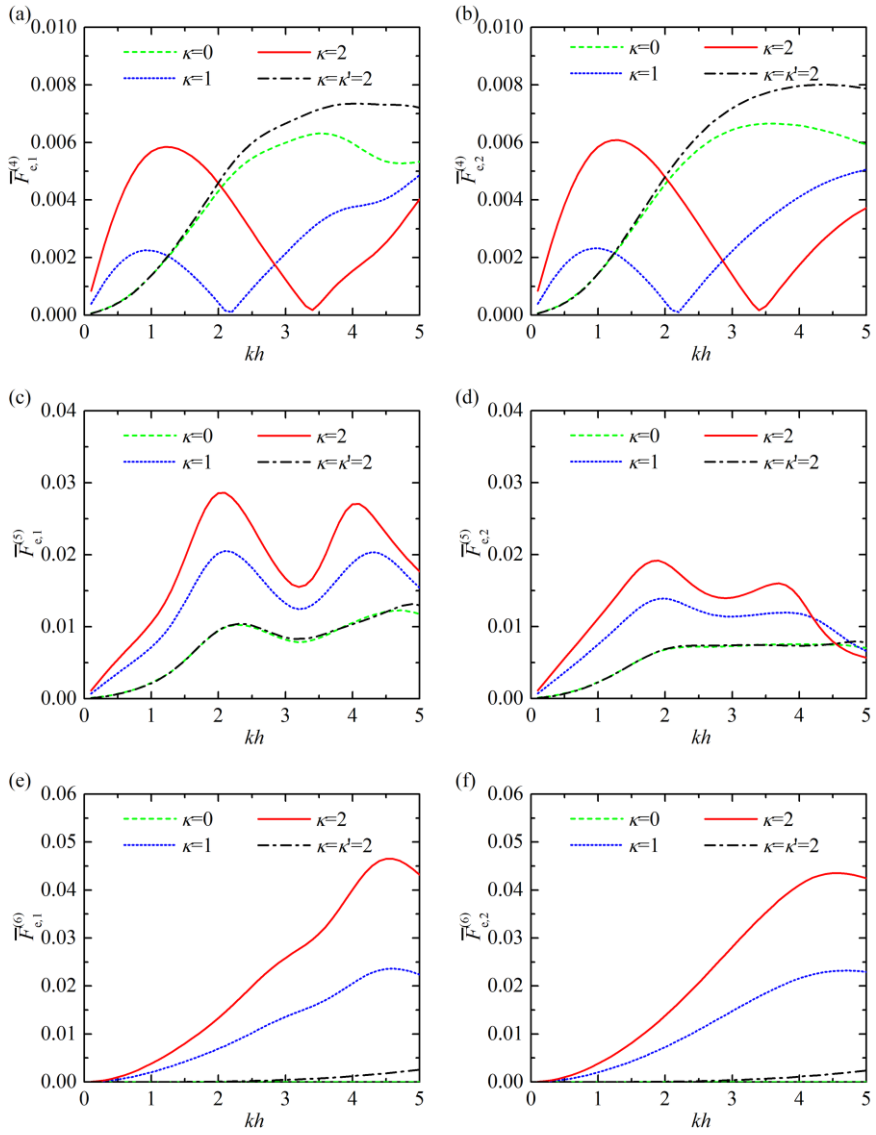

Fig. 15. Normalised wave excitation forces acting on the two caissons vs. *kh* for four shapes of cross section: (a) $\overline{F}^{(4)}_{e,1}$; (b) $\overline{F}^{(4)}_{e,2}$; (c) $\overline{F}^{(5)}_{e,1}$; (d) $\overline{F}^{(5)}_{e,2}$; (e) $\overline{F}^{(6)}_{e,1}$; (f) $\overline{F}^{(6)}_{e,2}$.

7 Conclusions

In this paper we developed an analytic model for the problem of wave diffraction from multiple truncated cylinders with arbitrary cross sections. Assuming the cylinders are subjected to regular waves of small steepness, linear potential flow theory is applied in the analytic model. The whole water domain is divided into interior regions below each cylinder and an exterior region representing the rest of the water domain. On this basis, the diffracted spatial velocity potential in these regions can be written as series of eigen-functions. The Fourier series method combined with the eigen-function expansion matching method are then used to satisfy the wetted surface body conditions and continuity conditions between adjacent regions, and to determine the unknown coefficients of the expressions of the diffracted spatial potential. Excellent agreement is found between the analytic results of wave excitations forces and moments and the numerical results obtained from a BEM-based code and the published data as well, which validates the analytic model. The model is then applied to study wave diffraction from two caissons and to

explore the effect of the incident wave angle, spacing between two caissons and configuration angle on the wave excitation forces and moments. Wave diffraction from the two identical caissons with some other shapes of cross section are also examined. The following conclusions may be drawn.

For two parallel caissons with the same dimensions located in a row, when incident waves propagate along the channel between them, i.e., $\beta = \pi/2$, the surge excitation force, pitch and yaw excitation moments acting on each caisson are triggered by the hydrodynamic interaction between the caissons. For different wave frequencies, changing the incident wave angle might play opposite roles, i.e., strengthening and weakening roles, on $\bar{F}_{e,1}^{(3)}$. For kh <3.8, the yaw excitation moments on both caissons for $\beta=\pi/4$ are larger than in the other cases (with different values of β).

Frequency responses of the surge, sway and heave excitation forces and also the pitch and yaw moments acting on Caisson 1 are found to oscillate around the $\bar{F}_{e,1}^{(i)}$-kh curve of isolated caisson case. This can be explained by the strengthening and weakening effects of the hydrodynamic interaction. As the spacing between the caissons increases, strengthening and weakening effects alternate at smaller intervals of kh.

As α increases from 0 to $\pi/2$ with $\beta = \pi/6$, the $\bar{F}_{e,1}^{(1)}$-kh and $\bar{F}_{e,1}^{(5)}$-kh curves change from double-peaked curves into single-peaked ones. With the increase of α, opposite effects of α on $\bar{F}_{e,1}^{(1)}$ and $\bar{F}_{e,1}^{(5)}$ might happen for different wave conditions. For most wave conditions, the cases with $\alpha=\pi/2$ and $\pi/3$ give the maximum and minimum values of $\bar{F}_{e,2}^{(2)}$ among the cases with five different value of α, respectively. The maximum value of $\bar{F}_{e,2}^{(2)}$ can be twice as large as that of the minimum for kh> 3.0. Whatever the value of α is, a minimum value of $\bar{F}_{e,1}^{(4)}$ occurs around kh=3.3. For kh ranging from 1.3 to 3.1, $\bar{F}_{e,2}^{(4)}$ is always the minimum and maximum for $\alpha=\pi/3$ and $\pi/2$, respectively, among the five cases. For short waves, e.g., kh>2.5, $\bar{F}_{e,2}^{(6)}$ with α=0 is much larger than in the other four cases, and it deserves more attention for stability.

The wave excitation forces/moments acting on each caisson in case κ=2 in surge, pitch and yaw modes are the largest among the case studies for the majority of the wave frequencies tested, and the wave excitation forces in the sway mode are the smallest. $\bar{F}_{e,1}^{(2)}$ and $\bar{F}_{e,2}^{(2)}$ for case $\kappa=\kappa'$=2 are the largest for the entire range of wave frequencies tested.

The research presented in this paper focused on wave diffraction from multiple stationary truncated cylinders. The analytic model established in this paper, together with that developed by Zheng, Zhang, Liu and Iglesias [41] for solving the problem of wave radiation from cylinders oscillating independently in the absence of an incident wave, can be used to calculate the hydrodynamic response of an array of truncated cylinders of arbitrary cross sections freely floating in water waves.

Acknowledgments

This research was supported by China Postdoctoral Science Foundation (Grant no. 2016M601041, 2017T100085), National Natural Science Foundation of China (51679124, 51879144) and Intelligent Community Energy (ICE), INTERREG V FCE, European Commission (Contract no. 5025).

References

[1] M. Lamas-Pardo, G. Iglesias, L. Carral, A review of very large floating structures (VLFS) for coastal and offshore uses, Ocean Eng, 109 (2015) 677-690.
[2] C.J.R. Garrett, Wave forces on a circular dock, Journal of Fluid Mechanics, 46 (1971) 129-139.
[3] J.L. Black, C.C. Mei, M.C.G. Bray, Radiation and Scattering of Water Waves by Rigid Bodies, Journal of Fluid Mechanics, 46 (1971) 151-&.
[4] X. Yu, A.T. Chwang, Analysis of wave scattering by submerged circular disk, J Eng Mech-Asce, 119 (1993) 1804-1817.
[5] B. Teng, D.Z. Ning, Wave diffraction from a uniform cylinder in front of a vertical wall, The Ocean Engineering, 21 (2003) 48-52.
[6] X. Yu, B. Zhang, An extended analytic solution for combined refraction and diffraction of long waves over circular shoals, Ocean Eng, 30 (2003) 1253-1267.
[7] B. Wu, Y. Zheng, Y. You, X. Sun, Y. Chen, On scattering and radiation problem for a cylinder over a cylindrical barrier in water of finite depth, Engineering Science, 6 (2004) 48-55.
[8] X.J. Niu, X.P. Yu, An analytic solution for combined wave diffraction and refraction around a vertical cylinder with idealized scour pit, Coast Eng, 67 (2012) 80-87.
[9] W. Finnegan, M. Meere, J. Goggins, The wave excitation forces on a truncated vertical cylinder in water of infinite depth, J Fluid Struct, 40 (2013) 201-213.
[10] D.Z. Ning, X.L. Zhao, B. Teng, L. Johanning, Wave diffraction from a truncated cylinder with an upper porous sidewall and an inner column, Ocean Eng, 130 (2017) 471-481.
[11] S. Zheng, Y. Zhang, Wave diffraction from a truncated cylinder in front of a vertical wall, Ocean Eng, 104 (2015) 329-343.
[12] S. Zheng, Y. Zhang, Wave radiation from a truncated cylinder in front of a vertical wall, Ocean Eng, 111 (2016) 602-614.
[13] F. Arena, Note on a paper by Ogilvie: the interaction between waves and a submerged horizontal cylinder, Journal of Fluid Mechanics, 394 (1999) 355-356.
[14] F. Arena, Interaction between long-crested random waves and a submerged horizontal cylinder, Physics of Fluids, 18 (2006).
[15] D. Pavone, F. Arena, Forces of random wave groups on vertical cylinders, 25th International Conference on Offshore Mechanics and Arctic EngineeringHamburg, Germany, 2006, pp. 249-253.
[16] H. Yu, S. Zheng, Y. Zhang, G. Iglesias, Wave radiation from a truncated cylinder of arbitrary cross section, Ocean Eng, 173 (2019) 519-530.
[17] H.S. Chen, C.C. Mei, Scattering and radiation of gravity waves by an elliptical cylinder, Department of Civil Engineering, MIT, 1971.
[18] A.N. Williams, Wave-forces on an elliptic cylinder, Journal of Waterway, Port, Coastal, and Ocean Engineering, 111 (1985) 433-449.
[19] H.S. Chen, C.C. Mei, Wave forces on a stationary platform of elliptical shape, Journal of Ship Research, 17 (1973) 61-71.
[20] A.N. Williams, Wave Diffraction by Elliptical Breakwaters in Shallow-Water, Ocean Eng, 12 (1985) 25-43.
[21] A.N. Williams, M.K. Darwiche, Three-dimensional wave scattering by elliptical breakwaters, Ocean Eng, 15 (1988) 103-118.
[22] S. Zhang, A.N. Williams, Wave scattering by submerged elliptical disk, Journal of Waterway, Port,

Coastal, and Ocean Engineering, 122 (1996) 38-45.
[23] A.M. Mansour, A.N. Williams, K.H. Wang, The diffraction of linear waves by a uniform vertical cylinder with cosine-type radial perturbations, Ocean Eng, 29 (2002) 239-259.
[24] J. Liu, A. Guo, H. Li, Analytical solution for the linear wave diffraction by a uniform vertical cylinder with an arbitrary smooth cross-section, Ocean Eng, 126 (2016) 163-175.
[25] J. Liu, A. Guo, Q. Fang, H. Li, H. Hu, P. Liu, Investigation of linear wave action around a truncated cylinder with non-circular cross section, Journal of Marine Science and Technology, 23 (2018) 866-876.
[26] N.B. Dişibűyűk, A.A. Korobkin, O. Yilmaz, Linear wave interaction with a vertical cylinder of arbitrary cross section: An asymptotic approach, Journal of Waterway, Port, Coastal, and Ocean Engineering, 143 (2017).
[27] S. Zhu, G. Moule, An efficient numerical calculation of wave loads on an array of vertical cylinders, Applied Mathematical Modelling, 20 (1996) 26-33.
[28] H. Kagemoto, D.K.P. Yue, Interactions among multiple three-dimensional bodies in water waves: an exact algebraic method, Journal of Fluid Mechanics, 166 (1986) 189-209.
[29] S. Alliney, Water waves diffraction around cylindrical obstacles, Applied Mathematical Modelling, 5 (1981) 237-240.
[30] O. Yilmaz, A. Incecik, Analytical solutions of the diffraction problem of a group of truncated vertical cylinders, Ocean Eng, 25 (1998) 385-394.
[31] O. Yilmaz, Hydrodynamic interactions of waves with group of truncated vertical cylinders, Journal of Waterway, Port, Coastal, and Ocean Engineering, 124 (1998) 272-279.
[32] P. Siddorn, R. Eatock Taylor, Diffraction and independent radiation by an array of floating cylinders, Ocean Eng, 35 (2008) 1289-1303.
[33] C.M. Linton, D.V. Evans, The interaction of waves with arrays of vertical circular cylinders, Journal of Fluid Mechanics, 215 (1990) 549-569.
[34] S. Zheng, Y. Zhang, Theoretical modelling of a new hybrid wave energy converter in regular waves, Renew Energ, 128A (2018) 125-141.
[35] S. Zheng, Y. Zhang, G. Iglesias, Wave-structure interaction in hybrid wave farms, J Fluid Struct, 83 (2018) 386-412.
[36] R. Eatock Taylor, On modelling the diffraction of water waves, Ship Technology Research, 54 (2007) 54-80.
[37] I.K. Chatjigeorgiou, S.A. Mavrakos, An analytical approach for the solution of the hydrodynamic diffraction by arrays of elliptical cylinders, Applied Ocean Research, 32 (2010) 242-251.
[38] I.K. Chatjigeorgiou, Three dimensional wave scattering by arrays of elliptical and circular cylinders, Ocean Eng, 38 (2011) 1480-1494.
[39] I.K. Chatjigeorgiou, The hydrodynamics of arrays of truncated elliptical cylinders, European Journal of Mechanics B/Fluids, 37 (2013) 153-164.
[40] J.T. Chen, J.W. Lee, A semi-analytical method for near-trapped mode and fictitious frequencies of multiple scattering by an array of elliptical cylinders in water waves, Physics of Fluids, 25 (2013) 097103.
[41] S. Zheng, Y. Zhang, Y. Liu, G. Iglesias, Wave radiation from multiple cylinders of arbitrary cross sections, Ocean Eng, 184 (2019) 11-22.
[42] M. Abramowitz, I.A. Stegun, Handbook of mathematical functions, Government Printing Office, Washington, D.C., 1964.
[43] M.E. Eidem, Overview of floating bridge projects in Norway, Proceedings of the ASME 2017

36th International Conference on Ocean, Offshore and Arctic EngineeringTrondheim, Norway, 2017.
[44] ANSYS-AQWA, Release. Vol. 14., ANSYS-Inc.Pennsylvania, USA, 2011.